

Recent progress on inverse design for integrated photonic devices: methodology and applications

Ruoyu Shen,^{a,b} Bingzhou Hong^{a,b,*}, Xiuyan Ren,^b Fenghe Yang,^b Wei Chu^{a,b,*},
Haiwen Cai,^{b,*} and Weiping Huang^{b,*}

^aFudan University, Department of Optical Science and Engineering, Shanghai, China

^bZhangjiang Laboratory, Shanghai, China

ABSTRACT. Photonic integrated circuits (PICs) have attracted great attention as promising platforms for high-data-rate communications and high-performance computing. For the PICs, photonic devices with compatible materials, compact footprint, high-performance, and sophisticated functionalities are necessary building blocks. Design optimization to implement such devices for target applications and requirements are of critical importance. In this respect, inverse design methods, including iterative optimizations and deep neural networks, have demonstrated significant advantages over the traditional simulation-based trial-and-error optimization approach. We provide an overview of the recent progress on the inverse designs for the integrated photonic devices. The principles and procedure of the inverse design methods are presented and discussed, followed by a summary of the methods employed for specific integrated photonic devices in different integrated photonics material platforms. Finally, topics of future applications and fabrication constraints for the inverse design methods are discussed.

© 2024 Society of Photo-Optical Instrumentation Engineers (SPIE) [DOI: [10.1117/1.JNP.18.010901](https://doi.org/10.1117/1.JNP.18.010901)]

Keywords: inverse design; integrated photonic devices; topology optimization

Paper 23082V received Jul. 24, 2023; revised Dec. 27, 2023; accepted Jan. 5, 2024; published Jan. 27, 2024.

1 Introduction

The concept of photonic integration was first proposed in 1969, with the anticipation that its realization would yield economic benefits.¹ In recent years, CMOS technology has significantly enhanced the capabilities of photonic integration, fulfilling expectations. Photonic integrated circuits (PICs) have already played a significant role in telecom,² data centers,³ and light detection and ranging.⁴ Moreover, they are demonstrating immense potential value in high-performance computing (HPC),⁵ biomedical sensing,⁶ optical coherence tomography,⁷ and other applications. Various photonic integration platforms based on different materials have emerged and achieved notable success in industrial applications, including silicon on insulator (SOI), lithium niobate on insulator (LNOI), silicon nitride (SiN), and SiO₂ planar lightwave circuit. A wide range of integrated photonic devices on different platforms have been designed and demonstrated, resulting in the formation of PICs with diverse performance capabilities.

Traditional designs of integrated photonic devices based on trial and error and parameter sweeping have been well-established. Generally, this approach always starts from a priori model calculated by numerical simulation algorithms such as finite-element method (FEM), finite-difference time-domain method, eigenmode expansion method, and rigorous coupled wave analysis. However, parameter sweeping is inefficient and lack of sufficient design degrees of freedom (DOF) which cannot meet the increasing demand for high-density integration and

*Address all correspondence to Bingzhou Hong, hongbz@zjlab.ac.cn; Wei Chu, chuwei@zjlab.ac.cn; Haiwen Cai, caihw@zjlab.ac.cn; Weiping Huang, huangwp@zjlab.ac.cn

low-loss transmission. To accelerate the design process and explore device performances, various inverse design methods have been proposed.^{8–11} Among these approaches, iterative optimization method and deep neural networks (DNN) emerge as two distinct categories of inverse design methods, each offering unique advantages and applicability. The iterative optimization method comprises global optimization algorithms, such as genetic algorithm (GA), particle swarm optimization (PSO), and direct binary search (DBS), as well as a local gradient-based method, such as the topology optimization (TO) method are also developed and demonstrated. These methods offer diverse searching strategies to achieve well-performing device structures more efficiently compared to traditional design methods. GA employs a searching strategy mimicking the biological evolution, while PSO conducts a strategy of group forage.^{12,13} Both methods are suitable for the inverse design of traditional empirical devices with limited DOF. DBS method for QR-code structure expands the design freedom to hundreds of degrees by segmenting the design area into hundreds of pixels.^{14,15} The refractive index of each pixel can be alternated between two different materials, such as Si and SiO₂ for silicon photonic devices. Superior structures can be found by DBS, yet brute-force search algorithms are tedious and time-consuming. To further expand DOF and improve inverse design efficiency, gradient-based TO methods are used to produce irregular structures.¹⁶ In this scheme, the optimization of material permittivity distribution within the design area, which is subdivided into smaller structural units, is performed using a gradient decent algorithm. The adjoint method,¹⁷ alternating direction method of multipliers optimization algorithm,^{18,19} and linear programming²⁰ are employed to calculate the shape gradient at each unit. Then, the permittivity in the design area is updated towards the direction of total gradient decent. The TO method, while leveraging the symmetry of Green's function to improve the efficiency of optimization process is limited by its high sensitivity to the initial designed structures.

In addition to iterative optimization method, DNN has also become a powerful tool for inverse design of integrated photonic devices. As a booming technology, DNNs have led to paradigm shift in many applications, including computer vision, image and speech recognition and nanophotonic device design.^{21–23} DNN establishes connections between device structures and the optical responses using training data set consisting of data features and labels. By employing forward networks, the optical response of integrated photonic devices can be accurately predicted, serving as a high-efficient approximation of numerical simulation in iterative optimization method. Another approach using DNN is the inverse model, in which optical responses are taken as inputs while device structures as outputs. Tandem network,²⁴ dimensionality reduction approaches^{25,26} and deep convolutional mixture density network²⁷ have been proposed to solve the issue of on-to-many relations in inverse model. The DNNs discussed above are primarily employed for the design of empirical device structures with limited DOF. On the other hand, generative models, such as generative adversarial networks (GAN), have been introduced to generate counter-intuitive irregular devices that exhibit exceptional performance.²⁸ Due to the rapid development of DNNs in other fields, many state-of-art networks such as Reinforcement learning have been increasingly employed in the inverse design of integrated photonic devices, showcasing significant potential for achieving high-performance designs.²⁹ All methods mentioned have been employed for designing different kinds of integrated photonic devices, which can be categorized into three structures implementations as illustrated in Fig. 1. The empirical structures, represented by red circles, typically have limited parameters and are always optimized by GA and PSO methods. The DBS method is employed only for QR-code structure, denoted by green circles. TO method is employed to generate irregular devices, as shown in yellow circles. In addition, the application of DNN has not yet been extensively explored in devices with complex functionalities, such as multiplexing systems, which deserve further investigation.

This article is organized as follows. Section 2 provides a comprehensive overview of inverse design methods, including the explanation of the principles and basic flow of the algorithms. The advantages, limitations, and scope of applications of these methods are also discussed. Section 3 focuses on the detailed applications of inverse design methods in various integrated photonic devices. Recent advances in inverse design methods for specific integrated photonic devices are summarized to provide a design guideline for designers seeking to explore novel integrated photonic devices utilizing inverse design approaches. Finally, the conclusion and outlook on future directions in this field are given in the last section.

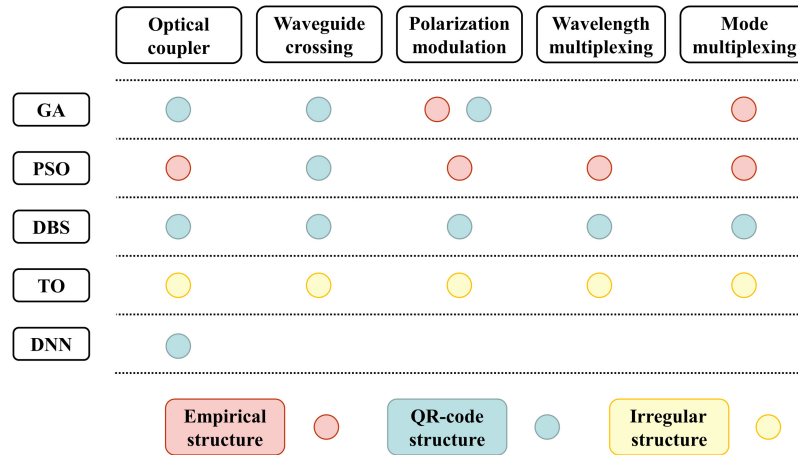


Fig. 1 Schematic demonstrating the applications of inverse design methods in different kinds of integrated photonic devices based on three different structure implementations. The empirical structure, QR-code structure and irregular structure are denoted by red, green, and yellow circles, respectively.

2 Iterative Optimization Method

2.1 Global Search Algorithm

GA as a global search algorithm employs the biological rule of survival-of-the-fittest to search for global optimal.³⁰ It has been used both in the inverse design of empirical structures and QR-code structures with different encoding ways of design area. For empirical structures, which have limited design parameters (such as length, port width, gap width, period, etc.) a vector of the abstracted parameters is optimized. For QR-code structure, the design area is divided into hundreds of pixels and a binary array representing the structure pixel distribution is generated where “0” represents one kind of material and “1” represents another. The implementation of GA method in QR-code structure significantly increases the design FOM which expands the application of GA method to more diverse devices. The optimization process of GA method is shown in Fig. 2(a). After randomly generating populations that represent different individual structures, the fitness of each individual, which indicates the figure of merit (FOM) is calculated. Then, a crossover operation is used, mimicking the way chromosomes exchange genetic information as Fig. 2(b) shows. An integer called “crossover point” is randomly selected to separate the individuals into upper and down sections and the two sections of two individuals are exchanged.

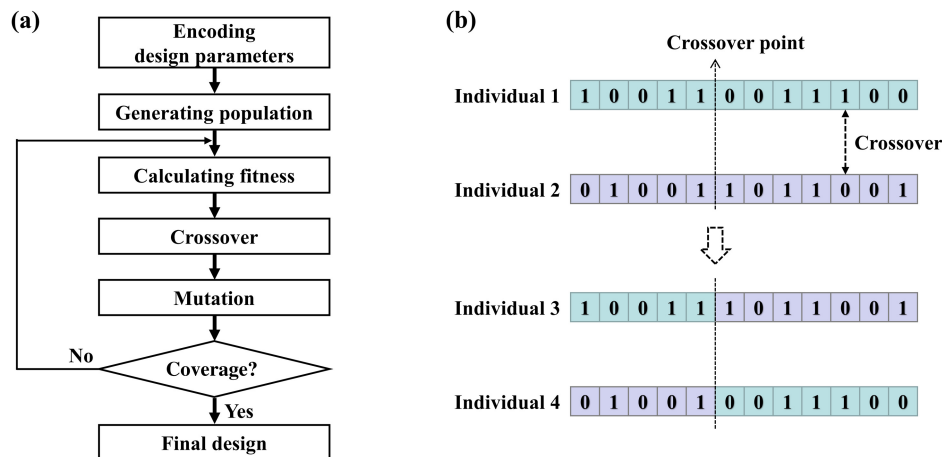


Fig. 2 Schematic of GA. (a) The optimization process of GA and (b) the crossover operation of GA algorithm.

Next, mutation operation is conducted to mimic the biological mutation which allows for the exploration of other design space. Several parameters of individuals are changed randomly. The selection of next generation is conducted after mutation. The loop of these operations iterates until convergence is achieved.

PSO is another global search algorithm inspired by the social behaviors like foraging of bird flock which has been widely applied to photonic devices optimization.⁸ In PSO process, particles are initialized at random positions with random velocities in the whole parameter space. Each particle represents one device structure. A designer defined FOM is used to evaluate the positions of each particle. The best position is defined as the best previous position PP_m and the best position during the whole iterations is defined as global position G . Then, the position and velocity of each particle are updated according to the following equations:

$$V_m^{k+1} = WV_m^k + c_1 \text{rand}_1(PP_m - X_m^k) + c_2 \text{rand}_2(G - X_m^k), \quad (1)$$

$$X_m^{k+1} = X_m^k + V_m^{k+1}. \quad (2)$$

The new velocity is impacted by the old velocity, the direction of the best previous position and the global position. W , called inertial weight determines how much a particle would stay at the old velocity. Cognitive rate c_1 determines the influence of each particle's previous best position. Social rate c_2 determines the effect of the global best position searched by the whole particle swarm. The random integers rand_1 and rand_2 reflect the unpredictable behavior of the flock. When the FOM of the global position meets the requirement, the iterations stop. The process of PSO is shown in Fig. 3(a). To expand the FOM, shape optimization can also be achieved by PSO using shape segmentation and digitization as Fig. 3(b) shows.³¹ The conventional Y-junction power splitter is divided into 13 sections with the same length. PSO was utilized to optimize the width of the 13 sections for small insertion loss. The splitter geometry is defined by spline interpolation of these 13 points.

DBS as a brute force searching method has been proven to be suitable for inverse design of QR-code structure. The device designed by DBS method is discretized into hundreds of pixels. Each pixel occupies two states: "0" represents SiO_2 or "1" represents Si. A pattern of pixel state distribution is first randomly generated as initial structure. Then, the state of each pixel is alternated. The FOM defined by designer is calculated after one state change. If the FOM is improved, the updated pixel state is retained. If not, the original pixel state is maintained and the state of next pixel is alternated. A single iteration is finished until all pixels have undergone a state change. The iterations continue until the FOM requirement is met. The process of DBS and the way of pixel state alternating are shown in Fig. 4. The DBS method increases the design FOM from a few parameters to hundreds of pixels which greatly extend the design of freedom thus improves the device performance. However, DBS is inefficient because of its brute-force searching

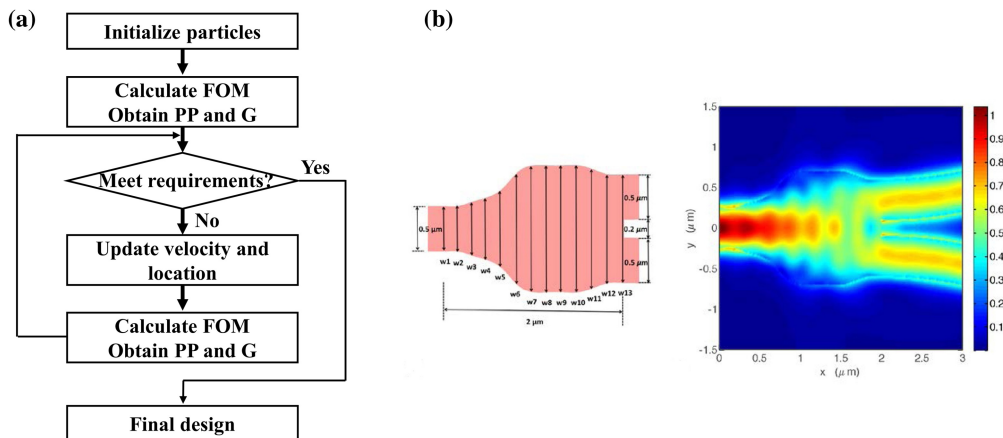


Fig. 3 (a) The optimization process of PSO. (b) Schematic of a Y-junction power splitter and simulated E-field distribution at 1550 nm wavelength from Ref. 31.

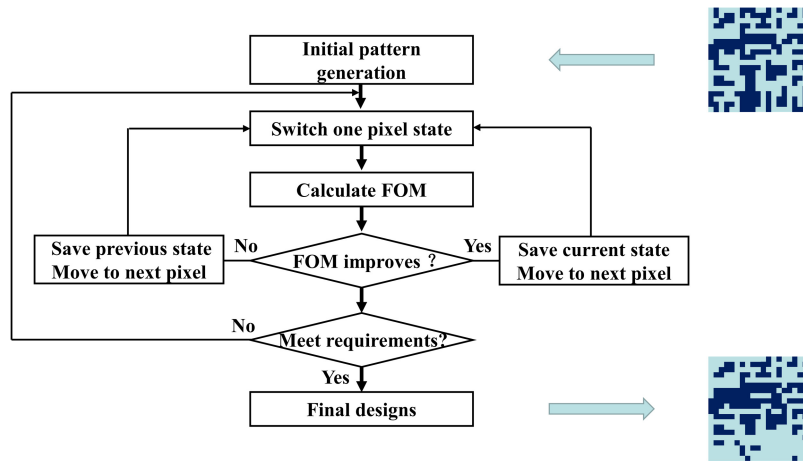


Fig. 4 Optimization process of DBS.

strategy. A variety of approaches to increase the computational efficiency have been proposed.³² The fabrication process of integrated photonic devices has limitation of smallest feature size. The size of pixel is the smallest feature size in QR-code structure optimized by DBS which can be determined by designer according to the fabrication requirement.

2.2 Local Gradient-Based Topology Optimization

As mentioned above, global search algorithms have been adopted to optimize empirical or QR-code structures with relatively small DOF compared to irregular structures. Irregular structure segments the design area into pixels as small as 10 or 20 nm which further increasing the DOF. Larger parameter space is brought by higher DOF to deal with more complicated designs, along with tremendous computation consumption. For global algorithms, the computation cost increases exponentially with the rise of variable parameters. Gradient-based methods alleviate the problem and become efficient solutions to the design of irregular structures with high DOF. However, one simulation is needed for calculation of gradient of each pixel in design area. The total calculation time scales up with the number of design parameters. To break the limits of design parameters, adjoint method has been proposed and applied.³³

Actually, adjoint methods have been applied in the optimization problems in many areas including mechanical engineering,³⁴ aerospace engineering,³⁵ and deep learning techniques.³⁶ In the field of photonic devices, adjoint method has been introduced to design various irregular structures which are introduced in Sec. 4. Adjoint method enables the calculation of gradient at each element in the design area with only two numerical simulations. To ensure the accuracy of the design and improve the overall efficiency of the optimization, an accurate and fast electromagnetic (EM) solver for two numerical simulations per iteration is indispensable and significant. A simple case can be considered to illustrate adjoint method as Fig. 5(a) shows in Ref. 17. The objective is to maximize the electric field intensity at a point x_0 , given a design area in which we can change the electric permittivity ϵ at each point x . With the FOM defined as $F = \frac{1}{2} |\mathbf{E}(x_0)|^2$, the change of FOM caused by a change of ϵ at one point x can be illustrated as $\delta F \approx \text{Re}[\overline{\mathbf{E}(x_0)^{\text{old}}} \delta \mathbf{E}(x_0)]$. $\delta \mathbf{E}(x_0)$ is the change of electric field intensity at x_0 triggered by the change of ϵ , which can be expressed as $\delta \mathbf{E}(x_0) = G(x_0, x) p(x)$. $G(x_0, x)$ is the Maxwell Green's function relating the electric field and polarization density $p(x)$. The Green function for Maxwell operator is symmetric: $G(x_0, x) = G(x, x_0)$ which is the underlying physical basis for realizing TO method. The change of FOM can be changed to

$$\delta F = \text{Re}[\overline{\mathbf{E}(x_0)^{\text{old}}} G(x_0, x) p(x)] = \text{Re}[G(x, x_0) \overline{\mathbf{E}(x_0)^{\text{old}}} p(x)] = \mathbf{E}^{\text{adjoint}}(x) p(x), \quad (3)$$

where $\mathbf{E}^{\text{adjoint}}(x) = G(x, x_0) \overline{\mathbf{E}(x_0)^{\text{old}}}$ is the fields of a dipole driven with amplitude $\overline{\mathbf{E}(x_0)^{\text{old}}}$. In second adjoint simulation, an electric dipole at x_0 with amplitude $\overline{\mathbf{E}(x_0)^{\text{old}}}$ is driven to provide $\mathbf{E}^{\text{adjoint}}(x)$ for all x . Therefore, δF at each point in the design area is now obtained by only two simulations.

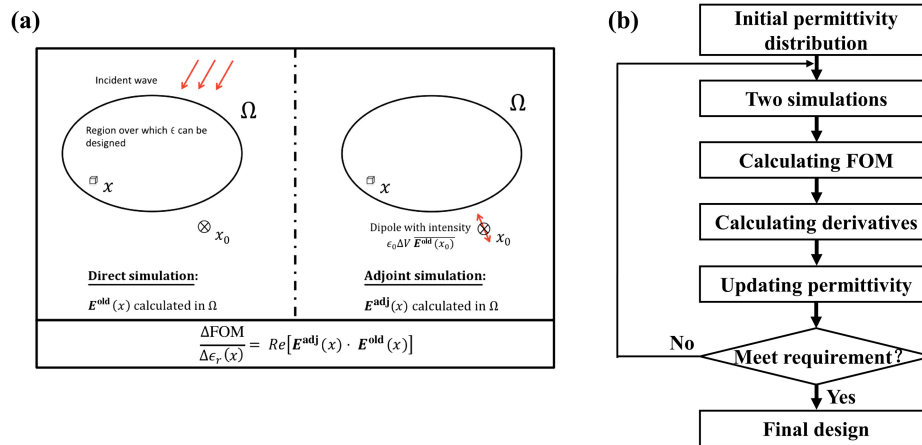


Fig. 5 (a) A simple case of using adjoint method through two simulations per iteration from Ref. 17. (b) The optimization process of TO based on adjoint method.

With adjoint method, gradient-based TO can be utilized to efficiently design irregular structures with high DOF. As Fig. 5(b) shows, the mapping between design parameters and permittivity distribution is specified and an initial distribution is determined. Then, forward and adjoint simulations are conducted to calculate the FOM gradient in each pixel of design area. Lastly, the design parameters are updated according to the gradients applying gradient decent methods. In TO method, density optimization³⁷ is adopted. Permittivity is operated as a continuous parameter for gradient computing which results in grayscale structure. For practical device, final optimized structure must exhibit binary features, so discretization operation is conducted. Multiple methods have been proposed for design discretization including artificial damping,³⁸ density filters,³⁹ penalty functions,⁴⁰ and other filters.⁴¹

3 Deep Neural Networks

3.1 Forward Model and Inverse Model Based on DNN

DNN has shown its great potential in various fields. In photonics, DNNs have already been widely used in the design of nano-antennas, optical filters, nano-lens, and metasurfaces.^{21–23} Forward model and inverse model based on DNN are two different ways contributing to device design as Fig. 6 shows. Forward model can predict optical responses fast and accurately after well training which is a great replacement of numerical simulation. It can accelerate the simulation speed and improve the inverse design efficiency since numerical simulations are the most time-consuming process in inverse design methods mentioned above. Forward model establishes a mapping between geometrical parameters and optical responses. A neuron is a basic unit that multiplies all the inputs by weights and adds them together with bias. The results pass through a nonlinear activation function. Multiple neurons form a hidden layer and the weights and biases of each neuron are network parameters to be trained for smaller loss using gradient descent

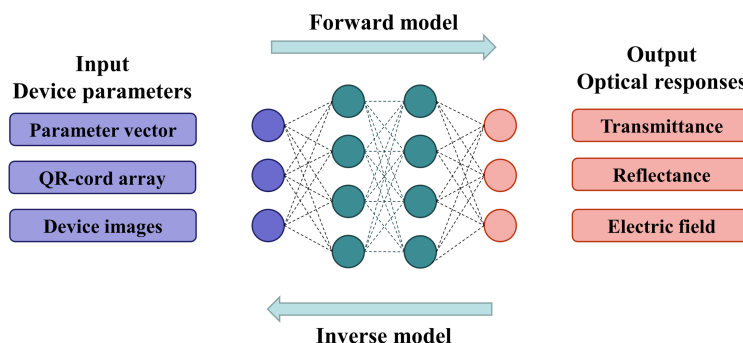


Fig. 6 The schematic of DNN used for the design of optical devices.

algorithm. The inverse model does not involve inverse design methods above, which realizes the inverse design of devices only by neural networks. The one-to-many relations make the realization hard because several geometries may result in similar responses. To solve the issue, tandem network,²⁴ dimensionality reduction approaches^{25,26} and deep mixture density network²⁷ have been proposed. Besides, generative models such as GAN are also inverse model which can generate counter-irregular devices.

The uses of neural networks has unique advantages when a series of devices with similar functions are required. However, precalculated datasets obtained from numerical simulations are always required for training, which consumes a lot of computing resources. To increase the data efficiency of photonic device optimization, physics-assisted NNs can be a promising option that employ physical knowledge on neural networks to reduce data requirements.⁴²⁻⁴⁴ Reinforcement learning, another booming optimization method, has also been applied in the design of various photonic devices, because it does not use a precomputed dataset but requires large computing resources for training networks.^{45,46}

Most of the DNN approaches mentioned above focus on solving the inverse design problem, another significant area is knowledge discovery that investigates the relation between design and response and revealing underlying physics insights.^{21,47} Dimensionality reduction,⁴⁸ manifold learning,⁴⁹ and explainable machine learning⁵⁰ have been applied to investigate the impact of input parameters and the importance of constituent parts of a structure with respect to its response.

4 Inversely Designed Devices

4.1 Optical Coupler

As a basic component of on-chip photon propagation, optical coupler plays an important role in the compact integration of photonic devices which is widely used in power splitting, wavelength division multiplexing and polarization separation. The insertion loss, bandwidth and crosstalk of optical coupler have great impact on the final performance of PICs. To obtain ultra-compact optical couplers with low loss and wide bandwidth, various inverse design methods have been adopted. In this section, power splitter, waveguide crossing, optical switch and optical router are mainly discussed. Optical diode and logical devices are also included in this section. Polarization beam splitter (PBS) is investigated in the section of polarization modulation devices.

4.1.1 Optical power splitter

Optical power splitter as one of the most basic building blocks of PICs has the function of dividing power. Device size, insertion loss, and bandwidth are always used to evaluate the performance of power splitter. To further improve device performance, various inverse design methods including GA, PSO, DBS, TO, and DNN have been used and the performance of these power splitters is shown in Table 1.

Yuan et al.⁵¹ designed arbitrary ratio splitters using GA method based on QR code structure. In order to implement GA method, the splitter was regarded as a 25-order matrix, in which each matrix element is a pixel as shown in Fig. 7(a). The state of a pixel can be alternated between Si for “1” and air for “0.” This work combined the QR-code structure and GA method by dividing and encoding the design area to obtain arbitrary ratio splitters with compact footprint and low excess loss.

With PSO method, an ultra-compact 3 dB power splitter based on Y-junction achieved an average insertion loss of 0.28 ± 0.02 dB with footprint of $1.2 \times 2 \mu\text{m}$.³¹ As demonstrated in Fig. 7(b), the Y-junction was divided into 13 sections with the same length and defined by spline interpolation of these 13 points. The widths of these 13 sections were used as the design parameters for PSO method. Shape optimization was realized in this case through shape segmentation and digitization which expands the design FOM. This scheme has become a paradigm. A traditional well-behaved device is taken as the initial structure and parameterized for PSO method. The discrete structure is interpolated when FOM needed to be calculated. The devices inversely designed by shape optimization using PSO method have large minimum feature size and can be fabricated by lithography.

Table 1 Examples of inversely designed optical power splitters.

Device	Structure	Method	Footprint	Fabrication	Performance (dB)
3 dB Splitter ⁵¹	QR-code	GA	2.5 × 2.5 μm	None	IL: 0.4 dB, BW: 30 nm
3 dB Splitter ³¹	Y-branch	PSO	1.2 × 2 μm	193 nm immersion lithography	IL: 0.28 ± 0.02 dB, BW: 80 nm
Splitter TE ₀ , TE ₁ ⁵²	QR-code	DBS	2.88 × 2.88 μm	EBL	IL: 1.5 dB, CT: -20 dB BW: 60 nm
3 dB Splitter ⁵³	QR-code	DBS	2.72 × 2.72 μm	EBL	IL: 0.7 dB, BW: 60 nm
Splitter TE ₀ , TE ₁ , TE ₂ ⁵⁴	QR-code	DBS	4 × 4.5 μm	EBL	IL: 1.5 dB, CT: -15 dB BW: 40 nm
1 × 2, 1 × 3 Splitter ⁵⁵	QR-code	DBS	3.6 × 3.6 μm	EBL	T: 80%, BW: 30 nm
1 × 2, 1 × 3 Splitter ⁵⁶	QR-code	DBS	3.8 μm-wide regular hexagon 4.0 μm-wide regular octagon	None	1 × 2: IL: 1.5 dB, BW: 100 nm 1 × 3: IL: 1.9 dB, CT: -15.5 dB BW: 100 nm
1 × 2 Splitter ⁵⁷	QR-code	DBS	2.4 × 2.4 μm 4.32 × 2.4 μm 2.4 × 3.6 μm	None	IL: 0.6 dB, BW: 100 nm IL: 0.6 dB, BW: 100 nm IL: 1.2 dB, BW: 100 nm
1 × 2 Splitter ¹⁷	Irregular	TO	2 × 2 μm	None	IL: 0.07 dB, BW: 100 nm
1 × 3 Splitter ⁵⁸	Irregular	TO	3.8 × 2.5 μm	EBL	IL: 0.642 dB, BW: 300 nm
1 × 2 Splitter ⁵⁹	QR-code	DNN	2.6 × 2.6 μm	None	T: 90%, BW: 200 nm
1 × 2 Splitter LNOI ⁶⁰	QR-code	GA	2.6 × 2.6 μm	None	IL: 0.2 dB, BW: 35 nm

With DBS method, a compact broadband dual-mode 3 dB power splitter was proposed with average excess loss and crosstalk <1.5 and -20 dB for both TE₀ and TE₁ modes.⁵² The inverse design area is composed of 24 × 24 pixels and each of them was a square of 120 × 120 nm with a circular hole of 45 nm radius as shown in Fig. 7(c). The FOM was defined to reduce insertion loss and crosstalk. The DBS method completely abandons traditional device structures and uses QR-code structure. Lu et al.⁵³ designed and fabricated a colorless 3 dB coupler with a near zero loss imbalance using DBS method. Xie et al.⁵⁴ demonstrated a compact 3 dB power splitter for TE₀, TE₁, and TE₂ modes using DBS method. The three-mode power splitter can directly split the mode multiplexed signals without demultiplexing devices. Xu et al. utilized DBS method to design 1 × 2 splitters with 1:1, 1:2, and 1:3 split ratios, and a 1 × 3 splitter with the ratio of 1:2:1⁵⁵ while Ma et al.⁵⁶ proposed arbitrary input 1 × 2 and 1 × 3 power splitters by DBS method based on symmetric structure. With DBS method, 1 × 2 power splitters with different output directions were designed and these splitters can be freely assembled to achieve arbitrary-direction, multi-channel, and ultra-compact power splitters.⁵⁷

With TO method based on level set method, an ultra-compact Y-splitter with footprints of 2 × 2 μm was optimized to obtain insertion loss of 0.07 dB in simulation as Fig. 7(d) shows.¹⁷ The optimal design was obtained within 51 iterations (102 simulations) while a design that has the same basis reached minimum insertion loss of 0.13 dB using PSO method after 1500 simulations. An order of magnitude difference in simulation times reflects the unique advantage of TO which is attributed to the fact that only TO actually utilizes the underlying physical principles to improve the utilization rate of simulation information. In Ref. 58, a broadband 1 × 3 splitter has been optimized by TO method and fabricated by EBL which achieved a measured insertion loss of 0.642 dB over the wavelength range of 1400–1700 nm as Fig. 6(e) shows. Piggott et al.

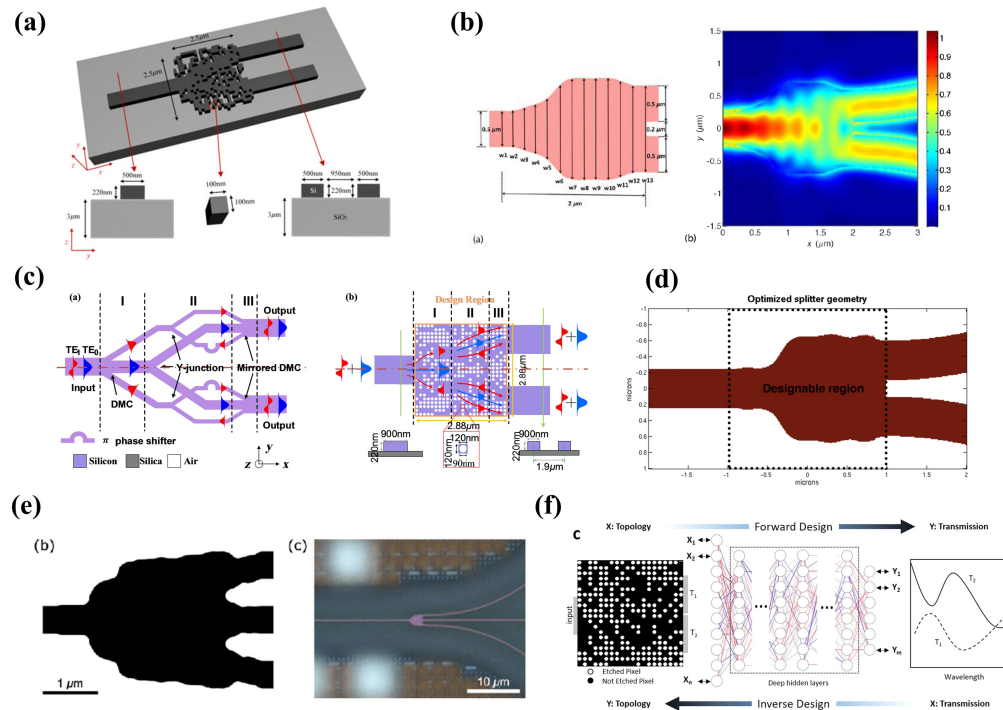


Fig. 7 Illustration of inversely designed power splitters. (a) Arbitrary ratio splitters designed by GA method from Ref. 51. (b) An ultra-compact 3 dB power splitter designed by PSO method from Ref. 31. (c) A compact broadband dual-mode 3 dB power splitter designed by DBS from Ref. 52. (d) An ultra-compact Y-splitter designed by TO method based on level-set method from Ref. 17. (e) A broadband 1×3 splitter optimized by TO method and fabricated by EBL from Ref. 58. (f) Power splitters with various target splitting ratios designed by DNN from Ref. 59.

eliminated the small features through curvature limiting and prevent the formation of gaps and bridges through morphological dilation and erosion operations.

DNNs have also been used to predict optical response of power splitters and inverse design the structures. In Ref. 59, power splitters with various target splitting ratios can be obtained using trained DNN in a fraction of a second as Fig. 7(f) shows. For forward prediction network, inputs were two-dimensional 20×20 arrays corresponding to the images of QR-code design areas and output was a vector including 63 spectral data points for transmission and reflection. For inverse design method, inputs and outputs were exchanged and Bernoulli log-likelihood classifier was used as loss function so that the inverse design could be treated as a classification problem.

Based on LNOI platform, an ultra-compact power splitter with low loss has been designed by GA method.⁶⁰ The device was designed on an LNOI wafer with a $0.6 \mu\text{m}$ LiNbO_3 layer on $2 \mu\text{m}$ SiO_2 . QR-code structure was adopted with pixel size of $130 \text{ nm} \times 130 \text{ nm}$ to achieve insertion loss as small as 0.2 dB in simulation.

4.1.2 Waveguide crossing

With the rapid development of the silicon photonics, the design and layout of an integrated system is becoming complex. The spatial waveguide crossings are inevitable for the large-scale planar optical interconnect system.⁶¹ For waveguide crossings, compact device footprint and polarization insensitivity are two significant design targets. Insertion loss and crosstalk are measured to evaluate the device performance. Traditional waveguide crossings realized by multi-mode interference⁶² and sub-wavelength gratings⁶³ have achieved low insertion loss and large crosstalk. However, inverse design methods have been adapted for compact footprint and more complex functionality such as multi-mode, high port density crossings demonstrated in Table 2.

A compact waveguide crossing has been inversely designed by GA based on 51×51 QR-code structure and fabricated to achieve an insertion loss $< 0.3 \text{ dB}$ and crosstalk $\leq 35 \text{ dB}$ for

Table 2 Examples of inversely designed waveguide crossing, router, and switch.

Device	Structure	Method	Footprint	Fabrication	Performance (dB)
TE ₀ Crossing ⁶⁴	QR-code	GA	5 × 5 μm	EBL	IL: < 0.3 dB, CT: < -35 dB
TE ₀ /TM ₀ Crossing ⁶⁵	QR-code	PSO	2 × 2 μm	None	TE: T: 69.1%, CT: -34.4 dB TM: T: 89.7 %, CT: -84.8 dB
Star Crossing ⁶⁶	QR-code	DBS	4 × 4: 7.1 μm	EBL	IL: 0.75 dB, CT: 22.5 dB
			5 × 5: 5.83 μm		IL: 0.9 dB, CT: 20 dB
			6 × 6: 7.3 μm		IL: 1.5 dB, CT: 18 dB
TE ₀ /TE ₁ Crossing ⁶⁷	QR-code	DBS	4.8 × 4.8 μm	EBL	IL: 0.6 dB, CT: -24 dB BW: 60 nm
TE ₀ /TE ₁ /TE ₂ Crossing ⁶⁸	QR-code	DBS	8 × 8 μm	EBL	IL: 0.28 dB, CT: -20 dB IL: 0.68 dB, CT: -20 dB IL: 0.82 dB, CT: -20 dB
Crossing ⁶⁹	Irregular	TO	3.36 × 3.36 μm	None	IL: <0.09 dB, CT: < -25.6 dB
Crossing LNOI ⁷⁰	Irregular	TO	12 × 12 μm	EBL	IL: 0.48 dB CT: <36 dB BW: 100 nm
Router ⁷¹	QR-code	GA	1.4 × 1.8 μm	FIB	Three ports T: 92%, 98%, 94%
Switch ⁷²	QR-code	DBS	1.2 × 2.4 μm	None	IL: <0.8 dB (a-GST)
					IL: >17.8 dB (c-GST)

fundamental TE mode.⁶⁴ The FOM is a combination of insertion loss and crosstalk for waveguide crossing. The final optimized design was fabricated by EBL after a fabrication-oriented optimization step in which the edged were smoothed and the corners were removed as Fig. 8(a) shows. QR-code structure has also been optimized by PSO method for TE and TM crossing with footprints of 2 × 2 μm.⁶⁵ A 3 × 3 crossing has been designed with the same footprint to further extend the functionality. Furthermore, 4 × 4, 5 × 5, and 6 × 6 star crossings demonstrated in Fig. 8(b) with high port densities have been inversely designed by DBS method and fabricated

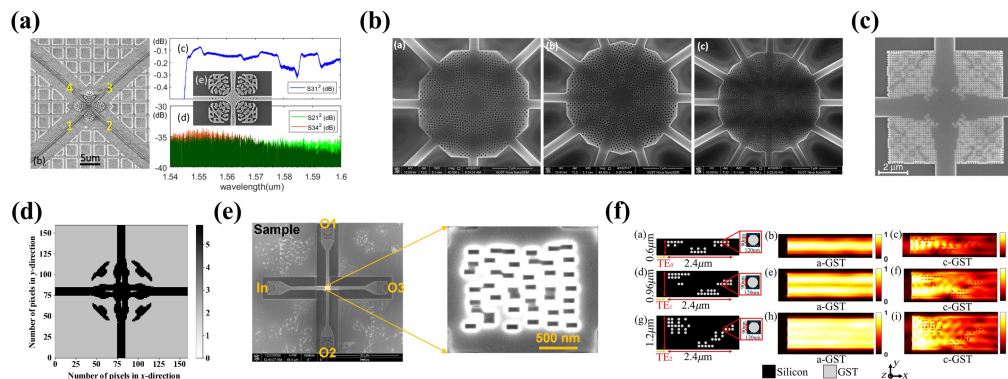


Fig. 8 Illustration of inversely designed waveguide crossings, router and switch. (a) A compact waveguide crossing based on QR-code optimized by GA method from Ref. 64. (b) 4 × 4, 5 × 5, and 6 × 6 star crossings with high port densities designed by DBS and fabricated in Ref. 66. (c) A three-mode crossing for TE₀, TE₁, and TE₂ mode designed by DBS method from Ref. 68. (d) TO optimized waveguide crossing from Ref. 69. (e) GA optimized optical router with ultra small footprint from Ref. 71. (f) Multimode optical switches with hybrid silicon-Ge₂Sb₂Te₅ platform designed by DBS from Ref. 72.

as Ref. 66 shows. In the mode-division multiplexed photonic circuits, multi-mode crossing is inevitable. Chang et al.⁶⁷ proposed and fabricated a compact dual-mode waveguide crossing designed by DBS method based on multi-mode interferometers (MMI) coupler. Liu et al.⁶⁸ designed and fabricated a three-mode crossing for TE₀, TE₁, and TE₂ mode using DBS method to construct a high-density integrated MDM photonic circuit as Fig. 8(c) shows. Apart from QR-code structure, Ref. 69 shows a crossing of irregular structure designed by TO method which has low insertion loss of 0.09 dB in simulation shown in Fig. 8(d). In this work, an adaptive projection method was proposed to solve the issue that TO method generates intermediate relative permittivity values. Based on LNOI platform, a compact waveguide crossing for TE₀ mode has been inversely designed by TO method and fabricated.⁷⁰ Inverse design of LNOI-based devices faces more challenges compared with SOI-based devices due to practical fabrication constraints. In this work, fabrication constraints of rib structures, minimum feature sizes and etched sidewalls of LNOI have been considered in the TO method.

An optical router as an essential component for photonic net on chip (NoC) can separate and assign incident signal to different output ports. In Ref. 71, GA algorithm has been utilized with FEM to inversely design a broadband three-channel wavelength routers with ultra-small footprint of $1.4 \times 1.8 \mu\text{m}$ and transmission as high as 98% as Fig. 8(e) shows. The positions and sizes of several basic structure cells with arbitrary shapes can be changed and optimized to maximize the output transmissions. The routing can be dynamically controlled via the application of appropriate patterns designed using DNNs in Ref. 73. A deep learning tandem network was used to design arbitrary transmission matrices using patterns of weakly scattering perturbations based on a multiport multi-mode waveguide.

Another key component of photonic NoC is optical switch, which can transmit or block optical signal. A multi-mode optical switches with hybrid silicon-Ge₂Sb₂Te₅ platform have been designed by DBS method demonstrated in Fig. 8(f).⁷² Compared to other SOI photonic devices inversely designed by DBS, the pixels in design area have two states of silicon or GST instead of silicon or air. The design target is minimizing the transmission of output in state of c-GST and maximizing the transmission of output in state of a-GST. Furthermore, integrated nonlinear optical switches have been designed by TO method based on different material platforms.^{74,75}

4.1.3 Optical diode

Optical diode that allows asymmetric light transmission is very attractive and useful for various photonic applications. The function of optical diode can be realized by break the Lorentz symmetry condition via spatial symmetry breaking when the functionality is limited to one input mode. Examples of optical diodes are based on meta-materials,⁷⁶ photonic crystals,⁷⁷ and ring resonators.⁷⁸ With higher design FOM of inverse design method, optical diodes can be realized by easier ways. Reference 79 demonstrated two optical diodes for TE and TM polarizations inversely designed by DBS method which show higher transmission efficiency and extinction ratio, large bandwidths and small footprint compared to alternatives. The design area is comprised of 30×30 pixels. The pixel is a square of $100 \times 100 \text{ nm}$ and the DBS method is used to maximize forward transmission efficiency and minimize the backward one. Another design of optical diode has been realized by TO method as Ref. 80 shows, forward transmission of 92.6% and backward one of 2.8% have been achieved with small footprint of $\sim 1.2 \times 2.4 \mu\text{m}$ in simulation. The optical diodes inversely designed show great advantages in device performances and generality and exhibit functionalities for other input modes due to the generality of inverse design method (Table 3).

Table 3 Examples of inversely designed optical diodes.

Device	Structure	Method	Footprint	Fabrication	Performance
Diode ⁷⁹	QR-code	DBS	$3 \times 3 \mu\text{m}$	FIB	TE: F: 62.1%, B: 2.8% TM: F: 79.8%, B: 10.4%
Diode ⁸⁰	Irregular	TO	$1.2 \times 2.4 \mu\text{m}$	None	Forward: 93.5%, Backward: 3.2%

Table 4 Examples of inversely designed optical logical devices.

Device	Structure	Method	Footprint	Fabrication	Performance (dB)
Logic ⁸⁵	QR-code	PSO	$1.2 \times 1.2 \mu\text{m}$	None	NOT AND
Logic ⁸⁶	Irregular	TO	$2.4 \times 2.4 \mu\text{m}$	None	AND OR NAND NOT

4.1.4 Optical logical devices

Optical logic gates based on SOI are believed to become a potential candidate for optical communication networks because of their low power consumption, high response speed, and small size.⁸¹ Instead of schemes such as interferometry,⁸² MZI⁸³ and semiconductor optical amplifiers (SOA)⁸⁴ used for optical logical devices, PSO and TO methods have been proposed to design optical logical devices. In Ref. 85, multi-objective PSO method has been utilized to design high-speed and ultra-compact all-optical NOT and AND gates on SOI platform. Four-port device structures with small footprint of $1.2 \times 1.2 \mu\text{m}$ lead to short respond time <25 ps. Reference 86 demonstrated AND, OR, NAND, and NOT logic gates on SOI platform by a multi-objective TO method. To design logic gate with multiple targets, subobjectives for each logic operation have been defined and summed. The footprint of each gate is ultracompact as small as $2.4 \times 2.4 \mu\text{m}$ (Table 4).

4.2 Spectral Modulation Devices

Spectral modulation devices including band-pass filters, narrow-band filters and wideband reflectors have many application scenarios in PICs, such as filtering of specific spectral wavelengths and wavelength multiplexing. Traditional on-chip spectral modulation devices based on microcavity, arrayed waveguide gratings (AWG) or other structures occupy large footprints. In this section, filters and reflectors with small footprints inversely designed by GA method are discussed.

4.2.1 Optical photonic filters

For optical filters on SOI platforms, inverse design methods have been used to engineer index distribution to modulate transmission spectra. A compact and scalable longpass filter was designed and fabricated to block light transmission in the stop band using GA method.⁸⁷ Light can pass through with a low insertion loss of 0.28 dB in the pass band. The photonic filter was based on SOI platform and inversely designed by two step GA algorithm. The QR-code structure consists of 51×51 pixels was optimized first by GA method and then the pixel pattern layout was adjusted slightly. In addition, the product of transmission rate in the pass band reflection rate in the stop band was set as the objective functions for optimization, which provides a solution to multiobjective optimization problems.

4.2.2 Optical reflector

Optical reflectors as an important component in integrated photonics are inevitable in laser cavities⁸⁸ and attenuators.⁸⁹ Distributed Bragg reflectors as widely used optical reflectors usually has large footprints.⁹⁰ For high-density on-chip integration, optical reflectors with small footprints are needed to be designed and fabricated. GA algorithm has been adopted to inversely design an ultracompact reflector with reflectivity higher than 97% and 1 dB bandwidth of 200 nm on SOI platform.⁹¹ The QR-code structure optimized was divided into 18×18 pixels with size of 120×120 nm which can be fabricated by EBL. With high reflectivity reflector, FP cavities with high-quality factors have also been fabricate (Table 5).

4.3 Polarization Modulation Devices

The SOIs platform provides a promising way of realizing high-density silicon photonic devices integration. However, the materials system with high refractive index contrast trigger highly

Table 5 Examples of inversely designed optical filter and reflector.

Device	Structure	Method	Footprint	Fabrication	Performance (dB)
Filter ⁸⁷	QR-code	GA	$5.1 \times 5.1 \mu\text{m}$	EBL	IL: 0.28, Blocked T: 25 dB
Reflector ⁹¹	QR-code	GA	$2.16 \times 2.16 \mu\text{m}$	EBL	Reflectivity: >95%
BW: 200 nm					

polarization-dependent performance of silicon photonic devices. A great solution to this issue is to use devices that can separately modulate different polarizations. Therefore, two passive on-chip polarization modulation devices including PBS and polarization rotator (PR) are of great significance for polarization multiplexing. Almost all of the inverse design methods have been conducted for PBS and PR due to their importance which are discussed in this section.

4.3.1 Polarization beam splitter

As a significant component to separate two polarizations, different device structures have been demonstrated and fabricated for the realization of PBS including MMIs,^{92,93} Mach-Zehnder interferometers (MZIs),⁹⁴ grating structures,^{95,96} and directional couplers (DCs).^{97,98} The PBSs based on MMIs, MZIs and grating structures achieve high polarization extinction ratio, but their footprints are large. DCs have been the most promising traditional structures for PBS devices for their compact sizes and easy fabrication process.⁹⁹ Since the traditional DCs have already achieved great performance, one type of inverse design solution is to fine-tune the DCs structure to further enhance performance without changing the overall implementation. Based on symmetric DCs, an ultrabroadband PBS using GA method has been presented to achieve insertion losses of 0.14 and 0.58 dB for TE and TM modes.¹⁰⁰ The optimized parameters were defined as the widths of and gaps between two waveguides at each section as shown in Fig. 9(a). Based on asymmetric DCs, PSO methods have been adopted to optimize the taper structure in the coupling region, which has the most important impact on final performance.^{101,103} The taper in Ref. 101 was segmented into 10 sections and the width of each section was defined as design parameters. The optimized PBS was fabricated to achieve a low insertion loss of 0.5 dB and high PER over 16.68 dB with small coupling length of $5 \mu\text{m}$ demonstrated in Fig 9(b).

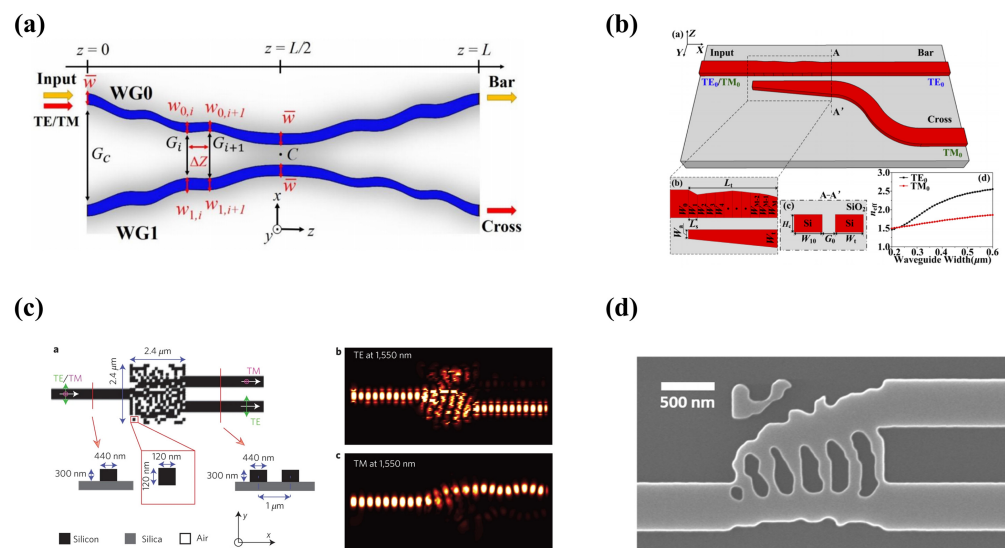


Fig. 9 Illustration of inversely designed PBSs. (a) A broadband PBS designed by GA based on symmetric DCs from Ref. 100. (b) PSO optimized PBS from Ref. 101. (c) A PBS with ultra-compact footprint designed by DBS and fabricated in Ref. 15. (d) PBS with footprint of $1.4 \times 1.4 \mu\text{m}$ optimized by TO method in Ref. 102.

Table 6 Examples of inversely designed PBSs.

Device	Structure	Method	Footprint	Fabrication	Performance
PBS ¹⁰⁰	Symmetric DC	GA	L: 50 μm	None	TE: IL: 0.14 dB, CT: -20.6 dB TM: IL: 0.58 dB, CT: -16.2 dB BW: 250 nm
PBS ¹⁰¹	Asymmetric DC	PSO	CL: 5 μm	Lithography	TE: IL < 0.5 dB, PER > 16.68 dB TM: IL < 0.46 dB, PER > 17.78 dB BW: 75 nm
PBS ¹⁰³	Asymmetric DC	PSO	CL: 15 μm	None	IL < 1.00 dB, PER > 30.00 dB BW: 90 nm
PBS ¹⁵	QR-code	DBS	2.4 \times 2.4 μm	Lithography	TE: T > 71%, PER > 11.8 dB TM: T > 80%, PER > 11.1 dB
PBS ¹⁰²	Irregular	TO	1.4 \times 1.4 μm	EBL	TE: IL: 0.82 dB, PER: 12 dB TM: IL: 2.10 dB, PER: 15 dB BW: 100 nm

To further reduce device size, DBS and TO methods have been proposed, which abandoned traditional structures. With DBS method on QR-code structure, a PBS with a footprint of $2.4 \times 2.4 \mu\text{m}$ has been designed and fabricated which is much smaller than traditional DCs structure shown in Fig. 9(c).¹⁵ Frandsen et al. further decreased PBS device size to $1.4 \times 1.4 \mu\text{m}$ with insertion loss lower than 0.82 and 2.1 dB and PERs better than 12 and 15 dB for TE and TM polarizations using TO method shown in Fig. 9(d).¹⁰² Frandsen also illustrated the trade-off between device size and performance. When using TO method, it is possible to control the device sizes to meet the requirement of device performance and integration density (Table 6).

4.3.2 Polarization rotator

As a key component of polarization diversity circuits, PRs have been widely investigated to rotate polarization from fundamental transverse electric mode to the fundamental transverse magnetic mode on-chip. Multiple structures have been attempted including DCs,^{104,105} subwavelength gratings¹⁰⁶ and double-stair waveguides.¹⁰⁷ Inverse design methods have been used to enlarge device bandwidth and reduce device footprint.

GA method has been used to design PR in Ref. 108. Two mode converters $\text{TE}_0 - \text{TE}_1$ and $\text{TE}_1 - \text{TM}_0$ were optimized first and then the combination of them was optimized using GA method based on QR-code structure. The fabricated devices are shown in Fig. 10(a). Guan et al.¹⁰⁹ demonstrated a compact PR designed by PSO method based on a bilevel-tapered TM_0 -to- TE_1 -mode converter and a novel TE_1 -to- TE_0 -mode converter shown in Fig. 10(b). Mode coupling scheme were conducted in these two cases. The TE_0 mode was first converted to high order mode and then transformed to the TM_0 mode. With DBS method, the QR-code structure was optimized to realize an equivalent asymmetric waveguide cross section, which excites the two hybridized modes to realize polarization rotation as Fig. 10(c) shows.¹¹⁰ The QR-code structure can be fabricated in single-step etching, which avoids the complex fabrication of asymmetric waveguide. In addition, the significant impact of initial patterns on final optimized device performances has been investigated. The optimized patterns from manually set initial patterns obtain higher FOMs than those from random initial patterns over the whole optimization process, which indicates that manually set initial patterns based on theoretical models can improve the optimized device performance. Majumder et al.¹¹¹ and Liu et al.¹¹³ have also adopted

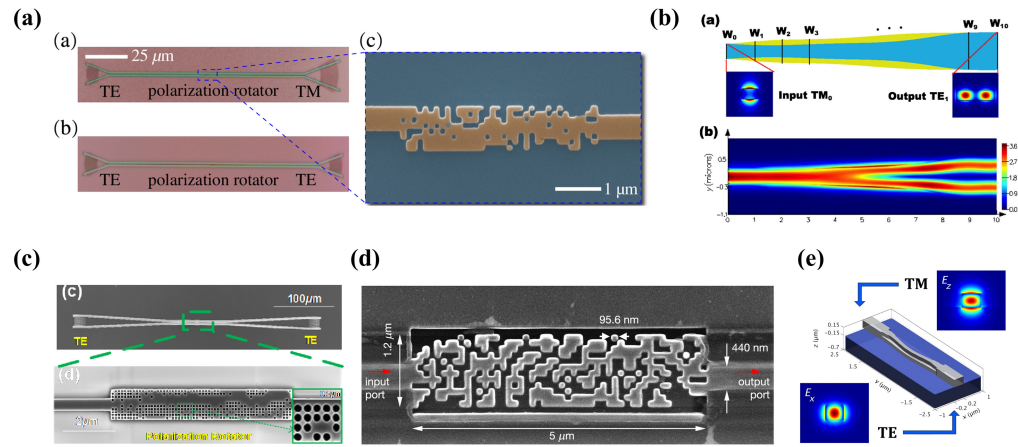


Fig. 10 Illustration of inversely designed PRs. (a) GA optimized PR fabricated by EBL in Ref. 108. (b) A compact PR based on bilevel taper designed by PSO from Ref. 109. (c) A QR-code PR fabricated in single-step etching designed by DBS in Ref. 110. (d) An ultra-compact PR optimized by DBS in Ref. 111. (e) A PR based on multilevel tapers designed by TO method in Ref. 112.

Table 7 Examples of inversely designed PRs.

Device	Structure	Method	Footprint	Fabrication	Performance
PR ¹⁰⁸	QR-code	GA	$0.96 \times 4.2 \mu\text{m}$	EBL	IL: 2.0 dB, PER: 10.0 dB, BW: 140 nm
PR ¹⁰⁹	Bent taper	PSO	L: $13.5 \mu\text{m}$	None	IL: 0.2 dB, PER: 25.0 dB, BW: 80 nm
PR ¹¹⁰	QR-code	DBS	$1.2 \times 7.2 \mu\text{m}$	EBL	IL: 0.7 dB, PER: 19.00 dB, BW: 60 nm
PR ¹¹¹	QR-code	DBS	$1.2 \times 5 \mu\text{m}$	EBL	T: 37%, PER: 9 dB, BW: 40 nm
PSR ¹¹³	QR-code	DBS	$2.4 \times 7.92 \mu\text{m}$	EBL	IL: 1 dB, PER: 20 dB, BW: 100 nm
PR ¹¹⁴	Irregular	TO	$1.2 \times 7 \mu\text{m}$	None	IL: 0.82 dB, CT < -18 dB, BW: 100 nm
PR ¹¹²	Irregular	TO	$1 \times 6 \mu\text{m}$	None	IL: 0.33 dB, PER: 30 dB, BW: 100 nm

DBS methods to design and fabricate ultra-compact PR and PSR. The ultracompact PR fabricated by EBL from Ref. 111 is shown in Fig. 10(d). TO methods have also been adopted to design PR in Refs. 112 and 114. Lebbe et al.¹¹² proposed a novel PR based on multilevel shape optimization shown in Fig. 10(e). The device shape was modified on two discrete levels along the etching direction, which led to higher conversion efficiency compared to single level structure (Table 7).

4.4 Wavelength Multiplexing System

When using silicon photonics, different optical wavelengths can be utilized to carry information which significantly increases the information transmission bandwidth. In wavelength division multiplexing systems, wavelength demultiplexer is the key passive device to separate different wavelength channels. Traditional wavelength demultiplexers such as AWG¹¹⁵ and ring resonator arrays¹¹⁶ suffer from high insertion loss, limited bandwidth and large footprint. So, inverse design methods of PSO and TO have been demonstrated to improve the performance of wavelength demultiplexer.

Ma et al.¹¹⁷ proposed a wavelength demultiplexer based on an adiabatic bent taper and a multi-mode waveguide optimized by PSO methods shown in Fig. 11(a). Twenty-seven parameters were used to characterize the entire device structure and low insertion loss of 0.25 dB was achieved. The length of the device was $15 \mu\text{m}$ which is competitive compared with traditional structures. However, the footprint can be further reduced with higher design FOM using TO method. Piggott et al.⁴⁰ experimentally demonstrated an ultra-compact wavelength demultiplexer

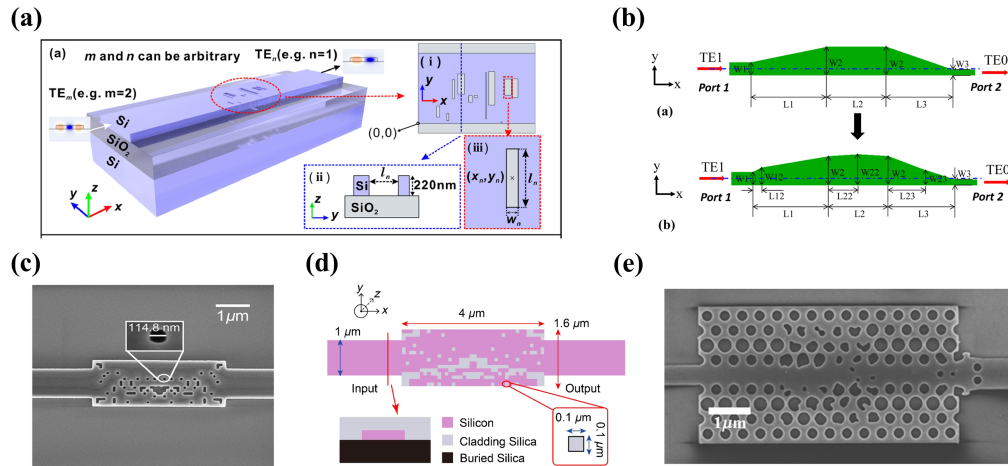


Fig. 11 Illustration of inversely designed wavelength demultiplexer. (a) A wavelength demultiplexer based on an adiabatic bent taper and a multi-mode waveguide optimized by PSO methods in Ref. 117. (b) A wavelength demultiplexer with footprint of $2.8 \times 2.8 \mu\text{m}$ optimized by TO method from Ref. 40. (c) A three-channel wavelength multiplexer optimized by TO method and fabricated in Ref. 118. (d) A four-channel wavelength multiplexer optimized by OB-1 method in Ref. 119.

with footprint of $2.8 \times 2.8 \mu\text{m}$ using TO method shown in Fig. 11(b). In this work, the truncated objective first method combined with steepest descent method was adopted. The designed wavelength multiplexer reached low loss of 2 dB and wide bandwidth over 100 nm with smallest footprint ever reported. Reference 118 proposed a compact three-channel wavelength demultiplexer to separate 1500, 1540, and 1580 nm light using TO method based on level-set method. To fabricate the devices successfully, a minimum radius of curvature constraint and a minimum gap constraint are applied to avoid small feature size. The curvature constraint was realized by periodically moving structure boundary under the curvature constraint level-set equation. Morphological dilation and erosion operations were adopted to realize gap constraint. After these operations, the optimized wavelength demultiplexer with ultra-small footprints of $5.5 \times 4.5 \mu\text{m}$ was fabricated successfully shown in Fig. 11(c). Han et al.¹¹⁹ designed a four-channel wavelength demultiplexer with compact footprint using objective-first (OB-1) method as demonstrated in Fig. 11(d). Based on SiN platform, a four-channel wavelength multiplexer with 30 nm channel spacing has been designed by TO method to achieve high transmission with small footprint (Table 8).¹²⁰

Table 8 Examples of inversely designed wavelength demultiplexers.

Device	Structure	Method	Footprint	Fabrication	Performance
1310/1550 nm ¹¹⁷	MMI	PSO	$2 \times 15 \mu\text{m}$	None	IL: 0.25 dB, CT: -20.00 dB BW: 90 nm
1300/1550 nm ⁴⁰	Irregular	TO	$2.8 \times 2.8 \mu\text{m}$	EBL	IL: 2.00 dB, CT: -11.00 dB BW: 100 nm
1500/1540/1580 nm ¹¹⁸	Irregular	TO	$5.5 \times 4.5 \mu\text{m}$	EBL	IL: 2.29 dB, CT: -10.7 dB
1453/1511/1576/1639 nm ¹¹⁹	Irregular	TO	$2.4 \times 8.4 \mu\text{m}$	None	IL: 1.87 dB, 2.10 dB, 1.68 dB, 1.74 dB CT: -14 dB, -13.2 dB, -13.7 dB, -16.1 dB
1490/1520/1550/1580 nm ¹²⁰	Irregular	TO	$6 \times 6 \mu\text{m}$	None	IL: 0.5 dB, 0.1 dB, 0.1 dB, 0.1 dB CT: -15 dB, -13.5 dB, -13 dB, -12 dB

4.5 Mode Multiplexing System

To meet the higher capacity requirements of on-chip PICs, mode division multiplexing has attracted tremendous interest because that it uses different optical modes as independent channels to transfer information, which can be combined with wavelength multiplexing to further expand data capacity.¹²¹ To realize mode multiplexing system, various mode-related devices have been investigated such as multimode bends,¹²² multimode crossings,¹²³ mode converters, and mode demultiplexers. Among them, mode converter and demultiplexer are two key components that have been inversely designed by various methods.

4.5.1 Mode converter

Many traditional structures have been adopted for mode converter including DC,¹²⁴ subwavelength gratings,¹²⁵ and MZIs.¹²⁶ Various inverse methods have also been investigated for mode converters. With adaptive GA method, a group of ultracompact and high-performance mode converters have been designed.¹²⁷ The positions and sizes of a series of rectangle nanoapertures were optimized as Fig. 12(a) shows. Based on an empirical single waveguide taper, the conversion between TE_1 , TE_2 , TE_3 , and TE_0 modes was achieved by shape optimization using PSO method demonstrated in Fig. 12(b).¹²⁸ The taper was segmented into several sections and the lengths and width of each section were used as parameters to be optimized, which is the commonly used approach to parameterize empirical structures. Guo et al.¹²⁵ used PSO method to design mode converters based on bricked subwavelength gratings. DBS methods have also been applied to design mode converter. Jia et al.¹²⁹ designed and fabricated a mode exchange device considering the axisymmetric constraint as shown in Fig. 12(c). A compact mode converter that can realize conversion from $TE_0 - TE_1$ and $TM_0 - TM_1$ simultaneously has been demonstrated experimentally using DBS method demonstrated in Fig. 12(d).¹³⁰ TO method based on OB-1 method has been utilized to inversely design mode converter in Ref. 19. $TE_0 - TE_1$ and $TM_0 - TM_1$ mode converters have been demonstrated with compact device sizes. Another case of TO method for mode converter was based on photonic crystal shown in Fig. 12(e).¹³¹ Based on LNOI platform, a mode converter for $TE_0 - TE_1$ conversion has been designed by TO method, which achieved a conversion efficiency of 93.46% (Table 9).¹³²

4.5.2 Mode (de)multiplexer

For mode demultiplexer, traditional device structures including asymmetric DCs,¹²⁴ asymmetric Y-branches¹³³ and MMIs¹³⁴ have been reported. DBS method based on asymmetric Y-branch has

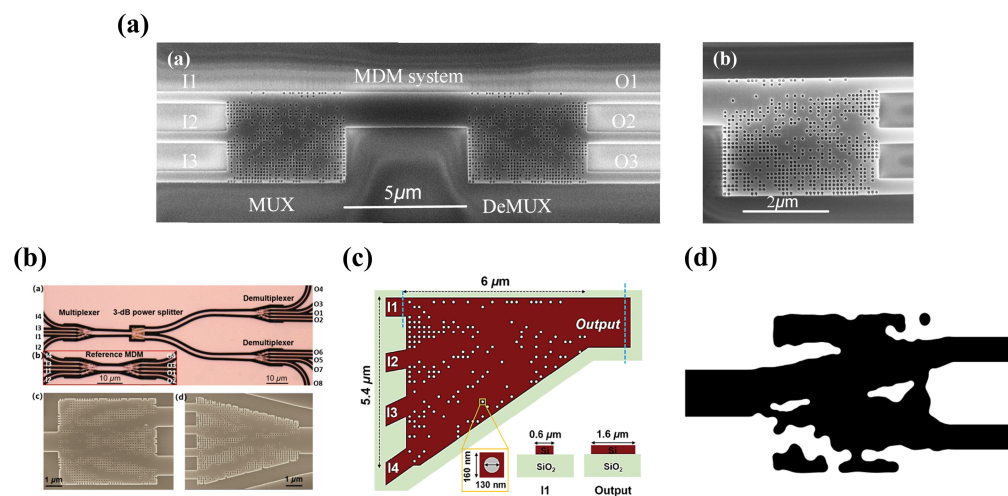


Fig. 12 Illustration of inversely designed mode converters. (a) A mode converter structure optimized by adaptive GA in Ref. 127. (b) Mode converters based on single waveguide taper designed by PSO in Ref. 128. (c) DBS optimized mode converter fabricated by EBL in Ref. 129. (d) A mode converter which can realize $TE_0 - TE_1$ and $TM_0 - TM_1$ conversion simultaneously optimized by DBS in Ref. 130. (e) A photonic crystal-based mode converter optimized by TO method in Ref. 131.

Table 9 Examples of inversely designed mode converters.

Device	Structure	Method	Footprint	Fabrication	Performance (dB)
$TE_0 - TE_1$	Rectangle apertures ¹²⁷	GA	$1.8 \times 2.2 \mu\text{m}$	None	IL: 0.48 dB, CT: -16.9 dB
$TE_0 - TE_2$					IL: 0.43 dB, CT: -15 dB
$TE_0 - TE_3$					IL: 1.4 dB, CT: -13 dB
$TE_0 - TE_4$					IL: 1.92 dB, CT: -10.9 dB
$TE_1 - TE_0$	Taper ¹²⁸	PSO	$4 \times 35 \mu\text{m}$	None	IL: 0.061 dB
$TE_2 - TE_0$					IL: 0.052 dB
$TE_3 - TE_0$					IL: 0.110 dB
$TE_0 - TE_1$	SWG Taper ¹²⁵	PSO	$9.39 \mu\text{m}$	None	IL < 1.0 dB
$TE_0 - TE_2$					CT < -15 dB
$TE_0 - TE_1$	QR-code ¹²⁹	DBS	$4 \times 1.6 \mu\text{m}$	EBL	T: 63%
$TE_0 - TE_1$	QR-code ¹³⁰	DBS	$4 \times 1.6 \mu\text{m}$	EBL	IL: 2.3 dB CT: -13.7 dB
$TM_0 - TM_1$					IL: 1.4 dB CT: -11.8 dB
$TE_0 - TE_1$	Irregular ¹⁹	TO	$1.6 \times 2.4 \mu\text{m}$	None	T: 86.4%
$TM_0 - TM_1$					T: 76.9%
$TE_0 - TE_1$	Irregular ¹³¹	TO	$6.3 \times 3.6 \mu\text{m}$	EBL	IL: 2 dB, ER: 21 dB
					BW: 43 nm
$TE_0 - TE_1$					T: 93.46%
$TE_0 - TE_1$	Irregular ¹³²	TO	$8 \times 3.6 \mu\text{m}$	None	T: 93.46%

LNOI

been implemented to design two modes and a three modes multiplexer, which occupy small footprints of $2.4 \times 3 \mu\text{m}$ shown in Fig. 13(a).¹³⁵ In Ref. 136, a four-modes multiplexer together with a multi-mode splitter have been designed by DBS and fabricated to realize an ultracompact mode division multiplexed PIC with footprints of $88 \times 25 \mu\text{m}$. In Ref. 137, a four-modes multiplexer has been demonstrated based on QR-code structure optimized by DBS. Two four-mode

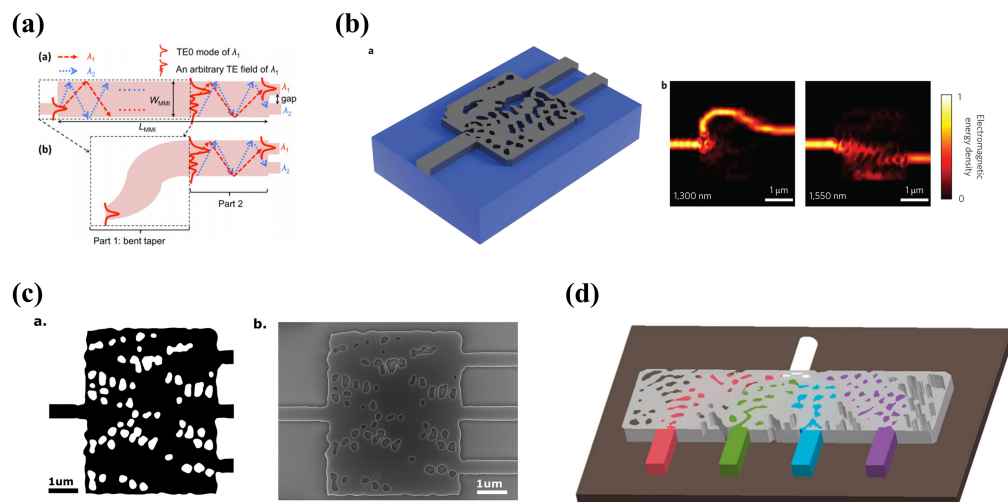


Fig. 13 Illustration of inversely designed mode (de)multiplexers. (a) DBS optimized three-modes multiplexer fabricated by EBL in Ref. 135. (b) A four-mode multiplexer together with a multi-mode splitter designed by DBS method in Ref. 136. (c) A four-mode multiplexer based on QR-code structure optimized by DBS method from Ref. 137. (d) TO optimized two-channel multiplexer in Ref. 58.

Table 10 Examples of inversely designed mode (de)multiplexers.

Device	Structure	Method	Footprint	Fabrication	Performance
TE ₀ , TE ₁	QR-code ¹³⁵	DBS	2.4 × 3 μm	None	IL < 1.00 dB, CT < -24.0 dB
TE ₀ , TE ₁ , TE ₂			3.6 × 4.8 μm		IL < 2.50 dB, CT < -19.0 dB
TE ₀ , TE ₁ ,	QR-code ¹³⁶	DBS	6.8 × 6 μm	EBL	IL < 1.40 dB, CT < -15.0 dB
TM ₀ , TM ₁					BW: 40 nm
TE ₀ , TE ₁ ,	QR-code ¹³⁷	DBS	5.4 × 6 μm	EBL	IL < 1.50 dB, CT < -14.6 dB
TE ₂ , TE ₃					BW: 60 nm
TE ₀ , TE ₁	Irregular ⁵⁸	TO	3.55 × 2.55 μm	Photolithography	IL < 1.00 dB, CT < -15.6 dB
					BW: 100 nm
TE ₀ , TE ₁	Irregular ⁷⁰	TO	12 × 12 μm	EBL	IL < 1.5 dB, CT < -15.8 dB
LNOI					BW: 80 nm

multiplexers are shown in Figs. 13(b) and 13(c). Reference 58 demonstrated a multiplexer of TE₀ and TE₁ mode designed by TO algorithm, which reached an average insertion loss of 1.0 dB over broad wavelength from 1500 to 1600 nm. The designed device is shown in Fig. 13(d). Based on LNOI platform, a mode multiplexer of TE₀ and TE₁ mode has been designed by TO method and fabricated in Ref. 70 (Table 10).

5 Comparison of Inverse Design Methods

We have discussed various integrated photonic devices obtained by different inverse design methods in the above subsections. As iterative optimization methods, both GA and PSO algorithms provide more efficient optimization strategies than traditional parameter sweeping, which can help to find the optimal structures in the parameter space faster. However, they rely on profound prior knowledge about the devices to be designed. The empirical initial structures and the key parameters that determine the device performance need to be known. So, the two methods are suitable for the design of those devices, which already have empirical structures with good performance such as 3 dB splitter based on y-branch, PBS based on symmetric DC and wavelength multiplexer based on MMI mentioned above. The devices based on empirical structure optimized by GA and PSO have small DOF and the final optimization result largely depends on the quality of the prior model. Fortunately, these methods are robust to manufacturing errors, because fine-tuning of empirical structures does not produce small feature structures that are difficult to be fabricated.

Compared to GA and PSO, DBS provides a method to segment the design domain into QR codes to improve the design DOF, but it adopts a brute force search optimization strategy, which is similar to parameter scanning. Because of much higher DOF, the devices designed by DBS can reach better performance with small footprints. However, the brute force search optimization strategy of DBS is inefficient and time-consuming because each structural update changes only one QR-code state and one forward simulation is needed. To reduce the optimization time, it is impossible for DBS methods to search the entire parameter space. The iteration is always early stopped when the set performance requirements are met. This is a trade-off that has to be made between device performance and optimization time. For optimization based on QR-code, random-generated and different initial structures are optimized to achieve best device performance.⁵² Initial structure based on a prior physical model is not necessary, but it significantly contribute to the fast convergence of global optimizations and the achievement of optimal device. For QR-code structure, the minimum feature size is the diameter of the design unit which is set at the beginning of the optimization. The diameter is generally designed over 80 nm to ensure that the

device can be manufactured, but the fabrication of holes with small diameters still introduces manufacturing error and device performance deterioration.

The TO algorithm further expands the DOF and improves the optimization efficiency. The trade-off is the possibility of producing structures of small feature sizes that are difficult to be manufactured. Compared to DBS method, TO method can significantly increase optimization efficiency using adjoint method based on the symmetry of Green's function. Only two simulations are needed in each iteration to calculate the gradient of each small pixel of design domain. The high DOF and fast optimization time make TO method promising for the design of integrated photonic devices with complicated functions. The wavelength multiplexers and mode multiplexers have been designed using TO method mentioned above. However, inappropriate initial structures may lead to undesired local optimal, since TO method is inherently gradient-based. When compact devices with complicated functionality are optimized, the optimization may not converge. Optimization of multiple random initial structures is a solution, but it increases the overall time and computational cost of one device design. OB-1 algorithm has been proposed to solve the problem.¹⁹ The design objectives are forced to be satisfied when Maxwell's equations are allowed to be violated. Then, alternating directions method of multipliers algorithm is used to minimize the physics residual.¹⁸ Besides, several advanced gradient optimizers such as sequential least squares programming¹³⁸ and method of moving asymptotes¹³⁹ can also be effective solutions. Furthermore, some researchers combine TO algorithm with machine learning to push the optimization out of its local optimal.¹⁴⁰ In addition, since the TO algorithm generates very small features and their sizes are different, how to improve its robustness to manufacturing errors has been extensively studied which is discussed in Sec. 6.

In addition to that iterative optimization method, DNNs have also been utilized in the inverse design of integrated photonic devices. The advantage of DNNs is that when a neural network is trained, it can generate a series of structures with similar functions but different targets quickly and easily. As the splitters mentioned in Sec. 4.4.1, structures of splitters with different splitting ratios can be generated by trained neural networks very fast. For other methods, each splitter with different splitting ratio needs a completely new optimization. However, an extra step of obtaining training dataset is needed for DNN compared to iterative optimization and it can be time-consuming. So, gradient-based methods would be a better option compared to DNN in cases where device with one specific target is required. However, reinforcement learning can be a great option in this case because it does not utilize a precomputed dataset but requires large computing resources for training networks.

The application between machine learning and PICs is interactive. Machine learning has been utilized for the design of integrated photonic devices as mentioned above. In the opposite direction, building neural networks on the platform of PICs holds the potential to address the computational demands of machine learning. This is due to the high-speed transmission and high energy efficiency of photons. Recently, multiple attempts have been made to realize all-optical DNN. Matrix multiplication and addition can be implemented fast and in parallel due to the noninteracting of photons. The optical nonlinearities can be used to realize the nonlinear functionality of NNs. This class of method to realize all-optical DNN always relies on hundreds of photonic components such as MZIs and phase-change materials.¹⁴¹⁻¹⁴³ However, the complexity of such approaches increases rapidly when the neural networks scale up. So, diffractive all-optical neural networks have been proposed to achieve the functionality of neural networks by analogously transmitting information through the diffraction of light in layered structures.¹⁴⁴⁻¹⁴⁶ The complex functional devices in all-optical neural networks rely on inverse design methods mentioned above. In the future, the efficiency of inverse design can also be further improved in all-optical neural networks.

6 Conclusion and Outlook

Inverse design methods provide a highly efficient approach to search the parameter space and maximize the theoretical performance of integrated photonic devices. In this article, we present a comprehensive summary of recent advancements in integrated photonic devices achieved through the utilization of inverse design methods, including iterative optimization methods and DNNs. The principles and workflows of GA, PSO, DBS, and TO have been introduced.

Moreover, we present an overview of the application of these methods to specific integrated photonic devices, including optical couplers, MDM devices, WDM devices, and other relevant devices. We list the device performances achieved by different inverse design methods for each specific device type.

Inverse design methods have already been implemented to design microwave devices and magnonic devices.^{147–149} The achievements in these areas serve as valuable references and can be adapted for the design of integrated photonic devices. In addition, the future holds great promise for leveraging inverse design to enhance the performance of active devices. By employing inverse design methods, we can unlock the full potential of active devices and push the boundaries of their performance. This approach enables us to optimize the intricate parameters and configurations of these devices, leading to improved efficiency, enhanced functionality, and higher levels of integration. The ability to tailor the design of active devices such as modulators, lasers, and isolators through inverse design provide exciting opportunities for advancing optical systems and enabling novel applications.¹⁵⁰

As inverse design plays an increasingly important role in the design of various kinds of optical devices, several issues need to be considered. One major concern is the fabrication challenges associated with inversely designed devices, which often exhibit small feature sizes and irregular-shaped structures that are difficult to fabricate in commercial semiconductor foundries. Currently, most of inversely designed integrated photonic devices are fabricated by high-resolution EBL or FIB techniques, which are costly, time-consuming, and not suitable for mass production in industry. Fortunately, the 12-inch silicon photonics technology at advanced process nodes (typically 40–65 nm) has been developed and made available for fabless companies, opening the possibility of inverse design methodologies adapted in commercial foundries. The integration of inverse design methodologies with commercial fabrication processes conditions holds the potential to address the challenges associated the mass production of inversely designed devices. Several approaches have been proposed to integrated the fabrication constraints in foundries for inversed design of photonic devices. Convolutional filters followed by thresholding have been introduced, but they may introduce smaller artifacts.¹⁵¹ Minimum gap and minimum radius of curvature constraints were introduced by Piggott et al.⁵⁸ to design and fabricate a series of devices using 193 nm immersion lithography. Hammond et al.¹⁵² proposed a TO method that incorporates constraints on minimum linewidth, linespacing, curvature, area, and enclosed-area “design rule check” constraints. Schubert et al.¹⁵³ introduced a novel method that combines a conditional generator that initialize binary states to occupy full design area and a straight-through gradient estimator for each single state while the optimization loop is turned on, ensuring that the designed devices satisfy stringent length scale constraints. These strategies aim to enable the fabrication of devices in commercial foundries by incorporating strict fabrication constraints into the TO process. The goal of inverse design is to fabricate devices in commercial foundries while the design FOM is maintaining. However, achieving this goal remains a pressing challenge for the widespread application of inversely designed integrated photonic devices in large-scale scenarios.

Another exciting topic in this field is the combination of different optimization methods in the inverse design of integrated photonic devices, particularly the integration of DNN with iterative optimization schemes. The use of DNNs for fast prediction of optical responses can replace the computationally expensive numerical simulations during the iterative optimization process. The combination of DNNs and GAs has been applied for the design of integrated photonic devices.¹⁵⁴ However, the application of deep learning in integrated photonic devices is currently limited to forward prediction of optical responses.^{155,156} Furthermore, other successful techniques from various fields, such as Tandem network,²⁴ reinforcement learning²⁹ and generative model.^{28,157} These techniques have demonstrated success in other domains and offer promising avenues for advancing the field of integrated photonic device design through inverse design methodologies.

Disclosures

The authors declare no conflicts of interest.

References

1. S. E. Miller, "Integrated optics - an introduction," *Bell Syst. Tech. J.* **48**, 2059–2069 (1969).
2. D. Thomson et al., "Roadmap on silicon photonics," *J. Opt.* **18**, 073003 (2016).
3. Z. P. Zhou et al., "Development trends in silicon photonics for data centers," *Opt. Fiber Technol.* **44**, 13–23 (2018).
4. W. Q. Xie et al., "Heterogeneous silicon photonics sensing for autonomous cars," *Opt. Express* **27**, 3642–3663 (2019).
5. T. F. de Lima et al., "Progress in neuromorphic photonics," *Nanophotonics* **6**, 577–599 (2017).
6. T. Hu et al., "Silicon photonic platforms for mid-infrared applications [Invited]," *Photonics Res.* **5**, 417–430 (2017).
7. B. I. Akca et al., "Integration on a microchip: a glimpse into the future of optical coherence tomography," *Prog. Opt.* **66**, 1–34 (2021).
8. S. M. Mao et al., "Inverse design for silicon photonics: from iterative optimization algorithms to deep neural networks," *Appl. Sci.* **11**, 3822 (2021).
9. S. D. Campbell et al., "Review of numerical optimization techniques for meta-device design [Invited]," *Opt. Mater. Express* **9**, 1842–1863 (2019).
10. S. Molesky et al., "Inverse design in nanophotonics," *Nat. Photonics* **12**, 659–670 (2018).
11. K. Yao et al., "Intelligent nanophotonics: merging photonics and artificial intelligence at the nanoscale," *Nanophotonics* **8**, 339–366 (2019).
12. J. H. Holland, "Genetic algorithms," *Sci. Am.* **267**, 66–72 (1992).
13. J. Robinson et al., "Particle swarm optimization in electromagnetics," *IEEE Trans. Antennas Propag.* **52**, 397–407 (2004).
14. M. A. Seldowitz et al., "Synthesis of digital holograms by direct binary search," *Appl. Opt.* **26**, 2788–2798 (1987).
15. B. Shen et al., "An integrated-nanophotonics polarization beamsplitter with $2.4 \times 2.4 \mu\text{m}^2$ footprint," *Nat. Photonics* **9**, 378–382 (2015).
16. J. S. Jensen et al., "Topology optimization for nano-photonics," *Laser Photonics Rev.* **5**, 308–321 (2011).
17. C. M. Lalau-Keraly et al., "Adjoint shape optimization applied to electromagnetic design," *Opt. Express* **21**, 21693–21701 (2013).
18. S. P. Boyd, *Distributed Optimization and Statistical Learning via the Alternating Direction Method of Multipliers*, p. 126, Now Publishers Inc., Hanover, Massachusetts (2011).
19. J. Lu et al., "Nanophotonic computational design," *Opt. Express* **21**, 13351–13367 (2013).
20. Y. Okamoto et al., "Material-density-based topology optimization with magnetic nonlinearity by means of stabilized sequential linear programming: SLPSTAB," *IEEE Trans. Magn.* **51**, 7207804 (2015).
21. P. R. Wiecha et al., "Deep learning in nano-photonics: inverse design and beyond," *Photonics Res.* **9**, B182–B200 (2021).
22. Z. C. Liu et al., "Tackling photonic inverse design with machine learning," *Adv. Sci.* **8**, 2002923 (2021).
23. J. Q. Jiang et al., "Deep neural networks for the evaluation and design of photonic devices," *Nat. Rev. Mater.* **6**, 679–700 (2021).
24. D. J. Liu et al., "Training deep neural networks for the inverse design of nanophotonic structures," *ACS Photonics* **5**, 1365–1369 (2018).
25. Y. Kiarashinejad et al., "Deep learning approach based on dimensionality reduction for designing electromagnetic nanostructures," *NPJ Comput. Mater.* **6**, 12 (2020).
26. M. Zandehshahvar et al., "Inverse design of photonic nanostructures using dimensionality reduction: reducing the computational complexity," *Opt. Lett.* **46**, 2634–2637 (2021).
27. R. Unni et al., "Deep convolutional mixture density network for inverse design of layered photonic structures," *ACS Photonics* **7**, 2703–2712 (2020).
28. C. Yeung et al., "Global inverse design across multiple photonic structure classes using generative deep learning," *Adv. Opt. Mater.* **9**, 2170079 (2021).
29. S. Hooten et al., "Inverse design of grating couplers using the policy gradient method from reinforcement learning," *Nanophotonics* **10**, 3843–3856 (2021).
30. D. Whitley, "A genetic algorithm tutorial," *Stat. Comput.* **4**, 65–85 (1994).
31. Y. Zhang et al., "A compact and low loss Y-junction for submicron silicon waveguide," *Opt. Express* **21**, 1310–1316 (2013).
32. B. Shen et al., "Integrated metamaterials for efficient and compact free-space-to-waveguide coupling," *Opt. Express* **22**, 27175–27182 (2014).
33. Y. Cao et al., "Adjoint sensitivity analysis for differential-algebraic equations: the adjoint dae system and its numerical solution," *SIAM J. Sci. Comput.* **24**, 1076–1089 (2003).
34. O. Sigmund et al., "Topology optimization approaches a comparative review," *Struct. Multidiscipl. Optim.* **48**, 1031–1055 (2013).
35. N. Aage et al., "Giga-voxel computational morphogenesis for structural design," *Nature* **550**, 84 (2017).

36. D. E. Rumelhart et al., “Learning representations by back-propagating errors,” *Nature* **323**, 533–536 (1986).
37. M. D. Zhou et al., “Minimum length scale in topology optimization by geometric constraints,” *Comput. Method Appl. Mech. Eng.* **293**, 266–282 (2015).
38. J. S. Jensen et al., “Topology optimization of photonic crystal structures: a high-bandwidth low-loss T-junction waveguide,” *J. Opt. Soc. Am. B* **22**, 1191–1198 (2005).
39. O. Sigmund, “On the design of compliant mechanisms using topology optimization,” *Mech Struct. Mach.* **25**, 493–524 (1997).
40. A. Y. Piggott et al., “Inverse design and demonstration of a compact and broadband on-chip wavelength demultiplexer,” *Nat. Photonics* **9**, 374 (2015).
41. B. Bourdin, “Filters in topology optimization,” *Int. J. Numer. Meth. Eng.* **50**, 2143–2158 (2001).
42. Y. Y. Chen et al., “Physics-informed neural networks for inverse problems in nano-optics and metamaterials,” *Opt. Express* **28**, 11618–11633 (2020).
43. I. Tanriover et al., “Physics-based approach for a neural networks enabled design of all-dielectric metasurfaces,” *ACS Photonics* **7**, 1957–1964 (2020).
44. C. Gigli et al., “Predicting nonlinear optical scattering with physics-driven neural networks,” *Appl Photonics* **8**, 026105 (2023).
45. I. Sajedian et al., “Optimization of colour generation from dielectric nanostructures using reinforcement learning,” *Opt. Express* **27**, 5874–5883 (2019).
46. D. Seo et al., “Structural optimization of a one-dimensional freeform metagrating deflector via deep reinforcement learning,” *ACS Photonics* **9**, 452–458 (2022).
47. Y. Kiarashinejad et al., “Knowledge discovery in nanophotonics using geometric deep learning,” *Adv. Intell. Syst.* **2**, 1900132 (2020).
48. D. Melati et al., “Mapping the global design space of nanophotonic components using machine learning pattern recognition,” *Nat. Commun.* **10**, 4775 (2019).
49. M. Zandehshahvar et al., “Manifold learning for knowledge discovery and intelligent inverse design of photonic nanostructures: breaking the geometric complexity,” *ACS Photonics* **9**, 714–721 (2022).
50. C. Yeung et al., “Elucidating the behavior of nanophotonic structures through explainable machine learning algorithms,” *ACS Photonics* **7**, 2309–2318 (2020).
51. Y. Xie et al., “Design of an arbitrary ratio optical power splitter based on a discrete differential multiobjective evolutionary algorithm,” *Appl. Opt.* **59**, 1780–1785 (2020).
52. W. J. Chang et al., “Inverse design and demonstration of an ultracompact broadband dual-mode 3 dB power splitter,” *Opt. Express* **26**, 24134–24143 (2018).
53. L. L. Z. Lu et al., “Inverse-designed single-step-etched colorless 3 dB couplers based on RIE-lag-insensitive PhC-like subwavelength structures,” *Opt. Lett.* **41**, 5051–5054 (2016).
54. H. C. Xie et al., “An ultra-compact 3-dB power splitter for three modes based on pixelated meta-structure,” *IEEE Photonic Technol. Lett.* **32**, 341–344 (2020).
55. K. Xu et al., “Integrated photonic power divider with arbitrary power ratios,” *Opt. Lett.* **42**, 855–858 (2017).
56. H. S. Ma et al., “Inverse-designed arbitrary-input and ultra-compact 1xN power splitters based on high symmetric structure,” *Sci. Rep.* **10**, 11757 (2020).
57. H. S. Ma et al., “Arbitrary-direction, multichannel and ultra-compact power splitters by inverse design method,” *Opt. Commun.* **462**, 125329 (2020).
58. A. Y. Piggott et al., “Inverse-designed photonics for semiconductor foundries,” *ACS Photonics* **7**, 569–575 (2020).
59. M. H. Tahersima et al., “Deep neural network inverse design of integrated photonic power splitters,” *Sci. Rep.* **9**, 1368 (2019).
60. Q. Xu et al., “Ultra-compact lithium niobate power splitters designed by an intelligent algorithm,” *Opt. Laser Technol.* **160**, 109057 (2023).
61. S. L. Wu et al., “State-of-the-art and perspectives on silicon waveguide crossings: a review,” *Micromachines* **11**, 326 (2020).
62. Y. Zhang et al., “Ultralow-loss silicon waveguide crossing using Bloch modes in index-engineered cascaded multimode-interference couplers,” *Opt. Lett.* **38**, 3608–3611 (2013).
63. S. L. Wu et al., “A compact and polarization-insensitive silicon waveguide crossing based on subwavelength grating MMI couplers,” *Opt. Express* **28**, 27268–27276 (2020).
64. P. F. Xu et al., “5x5 μm^2 compact waveguide crossing optimized by genetic algorithm,” in *Asia Commun. Photonics* (2017).
65. X. G. Yuan et al., “Ultra-compact multichannel optical waveguide crossings designed by a particle swarm optimized method,” *Opt. Commun.* **503**, 127458 (2022).
66. L. L. Z. Lu et al., “Inverse-designed ultra-compact starcrossings based on PhC-like subwavelength structures for optical intercross connect,” *Opt. Express* **25**, 18355–18364 (2017).

67. W. J. Chang et al., "Ultracompact dual-mode waveguide crossing based on subwavelength multimode-interference couplers," *Photonics Res.* **6**, 660–665 (2018).
68. Y. J. Liu et al., "Arbitrarily routed mode-division multiplexed photonic circuits for dense integration," *Nat. Commun.* **10**, 3263 (2019).
69. H. Liang et al., "Topological inverse design of fabrication-constrained nanophotonic devices via an adaptive projection method," *Opt. Lett.* **47**, 5401–5404 (2022).
70. C. F. Shang et al., "Inverse-designed lithium niobate nanophotonics," *ACS Photonics* **10**, 1019–1026 (2023).
71. Z. H. Liu et al., "Integrated nanophotonic wavelength router based on an intelligent algorithm," *Optica* **6**, 1367–1373 (2019).
72. H. S. Ma et al., "Inverse-designed single-mode and multi-mode nanophotonic waveguide switches based on hybrid silicon-Ge₂Sb₂Te₅ platform," *Results Phys.* **26**, 104384 (2021).
73. N. J. Dinsdale et al., "Deep learning enabled design of complex transmission matrices for universal optical components," *ACS Photonics* **8**, 283–295 (2021).
74. H. Chen et al., "Inverse-designed integrated nonlinear optical switches," *Laser Photonics Rev.* **16**, 2200254 (2022).
75. T. W. Hughes et al., "Adjoint method and inverse design for nonlinear nanophotonic devices," *ACS Photonics* **5**, 4781–4787 (2018).
76. Y. D. Xu et al., "Broadband asymmetric waveguiding of light without polarization limitations," *Nat. Commun.* **4**, 2561 (2013).
77. Y. Y. Zhang et al., "One-way optical transmission in silicon grating-photonic crystal structures," *Opt. Lett.* **39**, 4934–4937 (2014).
78. L. Fan et al., "An all-silicon passive optical diode," *Science* **335**, 447–450 (2012).
79. B. Shen et al., "Integrated digital metamaterials enables ultra-compact optical diodes," *Opt. Express* **23**, 10847–10855 (2015).
80. F. Callewaert et al., "Inverse design of an ultra-compact broadband optical diode based on asymmetric spatial mode conversion," *Sci. Rep.* **6**, 32577 (2016).
81. D. A. B. Miller, "Are optical transistors the logical next step?," *Nat. Photonics* **4**, 3–5 (2010).
82. P. P. Sahu, "All-optical switch using optically controlled two mode interference coupler," *Appl. Opt.* **51**, 2601–2605 (2012).
83. Y. A. Zaghoul et al., "Complete all-optical processing polarization-based binary logic gates and optical processors," *Opt. Express* **14**, 9879–9895 (2006).
84. X. L. Zhang et al., "All-optical AND gate at 10 Gbit/s based on cascaded single-port-coupled SOAs," *Opt. Express* **12**, 361–366 (2004).
85. Q. C. Lu et al., "High-speed ultra-compact all-optical NOT and AND logic gates designed by a multi-objective particle swarm optimized method," *Opt. Laser Technol.* **116**, 322–327 (2019).
86. B. Neseli et al., "Inverse design of ultra-compact photonic gates for all-optical logic operations," *J. Phys. D-Appl. Phys.* **55**, 215107 (2022).
87. P. F. Xu et al., "Scaling and cascading compact metamaterial photonic waveguide filter blocks," *Opt. Lett.* **45**, 4072–4075 (2020).
88. S. R. Selmic et al., "Single frequency 1550-nm AlGaInAs-InP tapered high-power laser with a distributed Bragg reflector," *IEEE Photonic Technol. Lett.* **14**, 890–892 (2002).
89. S. T. Chen et al., "Variable optical attenuator based on a reflective Mach-Zehnder interferometer," *Opt. Commun.* **361**, 55–58 (2016).
90. Y. Wang et al., "Ultra-broadband, compact, and high-reflectivity circular Bragg grating mirror based on 220 nm silicon-on-insulator platform," *Opt. Express* **25**, 6653–6663 (2017).
91. Z. J. Yu et al., "Genetically optimized on-chip wideband ultracompact reflectors and Fabry-Perot cavities," *Photonics Res.* **5**, B15–B19 (2017).
92. X. W. Guan et al., "Extremely small polarization beam splitter based on a multimode interference coupler with a silicon hybrid plasmonic waveguide," *Opt. Lett.* **39**, 259–262 (2014).
93. X. Sun et al., "Realization of an ultra-compact polarization beam splitter using asymmetric MMI based on silicon nitride/silicon-on-insulator platform," *Opt. Express* **25**, 8296–8305 (2017).
94. D. X. Dai et al., "Compact polarization beam splitter using an asymmetrical mach-zehnder interferometer based on silicon-on-insulator waveguides," *IEEE Photonic Technol. Lett.* **24**, 673–675 (2012).
95. H. Y. Qiu et al., "Broad bandwidth and large fabrication tolerance polarization beam splitter based on multimode anti-symmetric Bragg sidewall gratings," *Opt. Lett.* **42**, 3912–3915 (2017).
96. M. L. Ma et al., "Sub-wavelength grating-assisted polarization splitter-rotators for silicon-on-insulator platforms (vol 27, page 17581, 2019)," *Opt. Express* **28**, 17122–17123 (2020).
97. H. Wu et al., "Ultra-broadband high-performance polarizing beam splitter on silicon," *Opt. Express* **25**, 6069–6075 (2017).
98. D. X. Dai et al., "Novel ultra-short and ultra-broadband polarization beam splitter based on a bent directional coupler," *Opt. Express* **19**, 18614–18620 (2011).

99. T. Y. Huang et al., "Compact polarization beam splitter assisted by subwavelength grating in triple-waveguide directional coupler," *Appl. Opt.* **58**, 2264–2268 (2019).
100. P. H. Fu et al., "Optimization for ultrabroadband polarization beam splitters using a genetic algorithm," *IEEE Photonics J.* **11**, 6600611 (2019).
101. W. W. Chen et al., "Ultra-compact and low-loss silicon polarization beam splitter using a particle-swarm-optimized counter-tapered coupler," *Opt. Express* **28**, 30701–30709 (2020).
102. L. H. Frandsen et al., "Inverse design engineering of all-silicon polarization beam splitters," *Proc. SPIE* **9756**, 97560Y (2016).
103. D. W. Wang et al., "Broadband and compact polarization beam splitter based on an asymmetrical directional coupler with extra optimizing designs," *Appl. Opt.* **58**, 8221–8226 (2019).
104. D. X. Dai et al., "Novel concept for ultracompact polarization splitter-rotator based on silicon nanowires," *Opt. Express* **19**, 10940–10949 (2011).
105. J. Wang et al., "Design of a SiO₂ top-cladding and compact polarization splitter-rotator based on a rib directional coupler," *Opt. Express* **22**, 4137–4143 (2014).
106. H. N. Xu et al., "Subwavelength-grating-assisted silicon polarization rotator covering all optical communication bands," *Opt. Express* **27**, 5588–5597 (2019).
107. A. B. Xie et al., "Efficient silicon polarization rotator based on mode-hybridization in a double-stair waveguide," *Opt. Express* **23**, 3960–3970 (2015).
108. Z. J. Yu et al., "Genetic-algorithm-optimized wideband on-chip polarization rotator with an ultrasmall footprint," *Opt. Lett.* **42**, 3093–3096 (2017).
109. H. Guan et al., "Ultracompact silicon-on-insulator polarization rotator for polarization-diversified circuits," *Opt. Lett.* **39**, 4703–4706 (2014).
110. W. J. Chang et al., "Inverse design of a single-step-etched ultracompact silicon polarization rotator," *Opt. Express* **28**, 28343–28351 (2020).
111. A. Majumder et al., "Ultra-compact polarization rotation in integrated silicon photonics using digital metamaterials," *Opt. Express* **25**, 19721–19731 (2017).
112. N. Lebbe et al., "High-efficiency and broadband photonic polarization rotator based on multilevel shape optimization," *Opt. Lett.* **44**, 1960–1963 (2019).
113. Y. J. Liu et al., "Subwavelength polarization splitter-rotator with ultra-compact footprint," *Opt. Lett.* **44**, 4495–4498 (2019).
114. R. A. De Paula et al., "Broadband and highly efficient integrated polarization rotator designed by topology optimization," *Appl. Opt.* **61**, 463–470 (2022).
115. K. Sasaki et al., "Arrayed waveguide grating of 70x60 μm² size based on Si photonic wire waveguides," *Electron. Lett.* **41**, 801–802 (2005).
116. M. S. Dahlem et al., "Reconfigurable multi-channel second-order silicon microring-resonator filterbanks for on-chip WDM systems," *Opt. Express* **19**, 306–316 (2011).
117. Y. J. Ma et al., "Design and optimization of a novel silicon-on-insulator wavelength diplexer," *Opt. Express* **22**, 21521–21528 (2014).
118. L. Su et al., "Inverse design and demonstration of a compact on-chip narrowband three-channel wavelength demultiplexer," *ACS Photonics* **5**, 301–305 (2018).
119. J. M. Han et al., "Inverse designed tunable four-channel wavelength demultiplexer," *Opt. Commun.* **465**, 125606 (2020).
120. P. Kumar et al., "Inverse design of SiN based wavelength demultiplexer," in *Int. Conf. Adv. in Technol. (ICONAT)*, pp. 1–5 (2023).
121. C. L. Li et al., "Multimode silicon photonics," *Nanophotonics* **8**, 227–247 (2019).
122. X. H. Jiang et al., "Low-loss and low-crosstalk multimode waveguide bend on silicon," *Opt. Express* **26**, 17680–17689 (2018).
123. W. J. Chang et al., "An ultracompact multimode waveguide crossing based on subwavelength asymmetric Y-junction," *IEEE Photonics J.* **10**, 4501008 (2018).
124. Y. H. Ding et al., "On-chip two-mode division multiplexing using tapered directional coupler-based mode multiplexer and demultiplexer," *Opt. Express* **21**, 10376–10382 (2013).
125. Z. Z. Guo et al., "Experimental demonstration of a flexible and high-performance mode-order converter using subwavelength grating metamaterials," *Opt. Express* **31**, 10744–10757 (2023).
126. C. L. Sun et al., "Integrated switchable mode exchange for reconfigurable mode-multiplexing optical networks," *Opt. Lett.* **41**, 3257–3260 (2016).
127. T. G. Ou et al., "Ultra-compact and ultra-broadband arbitrary-order silicon photonic multi-mode converter designed by an intelligent algorithm," *Opt. Express* **31**, 9481–9495 (2023).
128. D. G. Chen et al., "Low-loss and fabrication tolerant silicon mode-order converters based on novel compact tapers," *Opt. Express* **23**, 11152–11159 (2015).
129. H. Jia et al., "Inverse-design and demonstration of ultracompact silicon meta-structure mode exchange device," *ACS Photonics* **5**, 1833–1838 (2018).

130. H. Jia et al., “Ultra-compact dual-polarization silicon mode-order converter,” *Opt. Lett.* **44**, 4179–4182 (2019).
131. L. H. Frandsen et al., “Topology optimized mode conversion in a photonic crystal waveguide fabricated in silicon-on-insulator material,” *Opt. Express* **22**, 8525–8532 (2014).
132. J. Peng et al., “A compact and low-loss te mode-order converter based on LNOI platform,” in *19th Int. Conf. Opt. Commun. and Networks (ICOON)*, pp. 1–3 (2021).
133. J. B. Driscoll et al., “Asymmetric Y junctions in silicon waveguides for on-chip mode-division multiplexing,” *Opt. Lett.* **38**, 1854–1856 (2013).
134. M. Y. Ye et al., “On-chip multiplexing conversion between wavelength division multiplexing-polarization division multiplexing and wavelength division multiplexing-mode division multiplexing,” *Opt. Lett.* **39**, 758–761 (2014).
135. W. J. Chang et al., “Ultra-compact mode (de) multiplexer based on subwavelength asymmetric Y-junction,” *Opt. Express* **26**, 8162–8170 (2018).
136. Y. J. Liu et al., “Ultra-compact mode-division multiplexed photonic integrated circuit for dual polarizations,” *J. Lightwave Technol.* **39**, 5925–5932 (2021).
137. H. C. Xie et al., “Highly compact and efficient four-mode multiplexer based on pixelated waveguides,” *IEEE Photonic Technol. Lett.* **32**, 166–169 (2020).
138. J. Nocedal et al., *Numerical Optimization*, Springer Series in Operations Research, 2nd ed., p. xxii, 664 p., Springer, New York (2006).
139. K. Svanberg, “The method of moving asymptotes - a new method for structural optimization,” *Int. J. Numer. Meth. Eng.* **24**, 359–373 (1987).
140. C. Yeung et al., “Enhancing adjoint optimization-based photonic inverse design with explainable machine learning,” *ACS Photonics* **9**, 1577–1585 (2022).
141. S. F. Xu et al., “High-order tensor flow processing using integrated photonic circuits,” *Nat. Commun.* **13**, 7970 (2022).
142. B. W. Dong et al., “Higher-dimensional processing using a photonic tensor core with continuous-time data,” *Nat. Photonics* **17**, 1080–1088 (2023).
143. J. Feldmann et al., “Parallel convolutional processing using an integrated photonic tensor core,” *Nature* **589**, 52 (2021).
144. X. Lin et al., “All-optical machine learning using diffractive deep neural networks,” *Science* **361**, 1004 (2018).
145. T. Yan et al., “All-optical graph representation learning using integrated diffractive photonic computing units,” *Sci. Adv.* **8**, eabn7630 (2022).
146. T. Z. Fu et al., “Photonic machine learning with on-chip diffractive optics,” *Nat. Commun.* **14**, 70 (2023).
147. M. Shadi et al., “Inverse design of compact power divider with arbitrary outputs for 5G applications,” *Sci. Rep.* **12**, 12844 (2022).
148. M. Sedaghat et al., “Compressed machine learning-based inverse model for the design of microwave filters,” in *IEEE MTT-S Int. Microwave Symp.*, pp. 13–15 (2021).
149. Q. Wang et al., “Inverse-design magnonic devices,” *Nat. Commun.* **12**, 2636 (2021).
150. J. H. Wang et al., “Adjoint-based optimization of active nanophotonic devices,” *Opt. Express* **26**, 3236–3248 (2018).
151. Y. Elesin et al., “Design of robust and efficient photonic switches using topology optimization,” *Photonic Nanostruct.* **10**, 153–165 (2012).
152. A. M. Hammond et al., “Photonic topology optimization with semiconductor-foundry design-rule constraints,” *Opt. Express* **29**, 23916–23938 (2021).
153. M. F. Schubert et al., “Inverse design of photonic devices with strict foundry fabrication constraints,” *ACS Photonics* **9**, 2327–2336 (2022).
154. Y. M. Ren et al., “Genetic-algorithm-based deep neural networks for highly efficient photonic device design,” *Photonics Res.* **9**, B247–B252 (2021).
155. D. Gostimirovic et al., “An open-source artificial neural network model for polarization-insensitive silicon-on-insulator subwavelength grating couplers,” *IEEE J. Sel. Top. Quantum. Electron.* **25**, 8200205 (2019).
156. X. Tu et al., “Analysis of deep neural network models for inverse design of silicon photonic grating coupler,” *J. Lightwave Technol.* **39**, 2790–2799 (2021).
157. T. Christensen et al., “Predictive and generative machine learning models for photonic crystals,” *Nanophotonics* **9**, 4183–4192 (2020).

Biographies of the authors are not available.